Cell Reports

Article

TDP1 mutation causing SCAN1 neurodegenerative syndrome hampers the repair of transcriptional DNA double-strand breaks

Graphical abstract

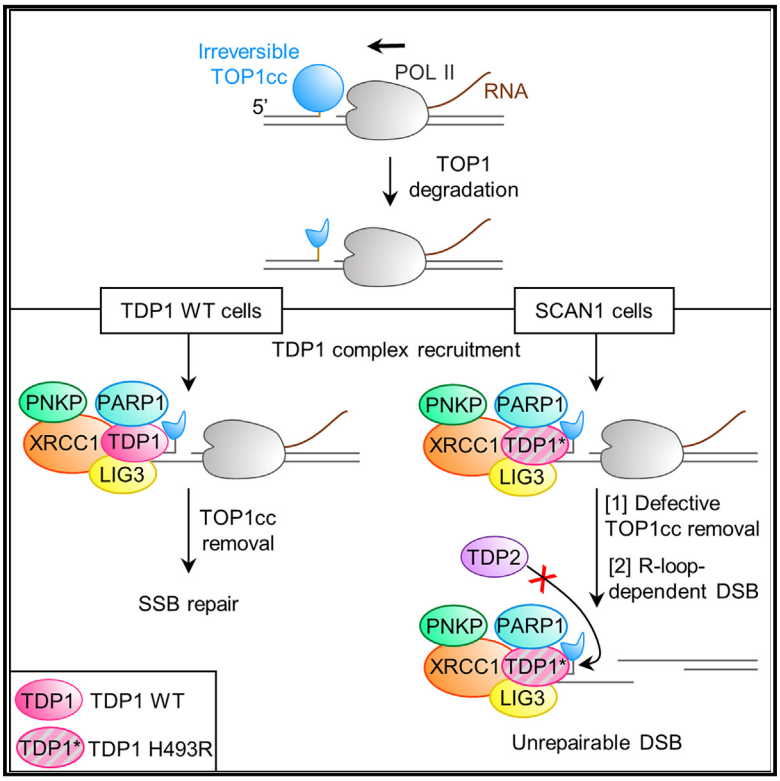

Highlights

- Generation of human SCAN1 cells with homozygous *TDP1* H493R mutation by CRISPR-Cas9
- SCAN1 cells accumulate TOP1ccs and G1 phase-specific transcriptional DSBs
- DSB accumulation in SCAN1 results from enhanced DSB formation and defective repair
- Mutated TDP1 protein hampers DSB repair by a TDP2-dependent backup pathway

Authors

Mathéa Geraud, Agnese Cristini, Simona Salimbeni, ..., Estelle Nicolas, Giovanni Capranico, Olivier Sordet

Correspondence

giovanni.capranico@unibo.it (G.C.), olivier.sordet@inserm.fr (O.S.)

In brief

Geraud et al. generate human SCAN1 cells by CRISPR-Cas9 to study SCAN1 disease. SCAN1 cells accumulate transcriptional DSBs specifically in G1 phase due to enhanced DSB formation and defective repair. The presence of mutated TDP1, rather than loss of its activity, causes defective repair by hampering a TDP2-dependent backup pathway.

Geraud et al., 2024, Cell Reports *43*, 114214
May 28, 2024
https://doi.org/10.1016/j.celrep.2024.114214

CellPress

Cell Reports

CellPress
OPEN ACCESS

Article

TDP1 mutation causing SCAN1 neurodegenerative syndrome hampers the repair of transcriptional DNA double-strand breaks

Mathéa Geraud,[1,5] Agnese Cristini,[1,5] Simona Salimbeni,[1,2,5] Nicolas Bery,[1] Virginie Jouffret,[3,4] Marco Russo,[2] Andrea Carla Ajello,[1] Lara Fernandez Martinez,[1] Jessica Marinello,[2] Pierre Cordelier,[1] Didier Trouche,[3] Gilles Favre,[1] Estelle Nicolas,[3] Giovanni Capranico,[2,6,*] and Olivier Sordet[1,6,7,*]

[1]Cancer Research Center of Toulouse (CRCT), INSERM, Université de Toulouse, Université Toulouse III Paul Sabatier, CNRS, 31037 Toulouse, France
[2]Department of Pharmacy and Biotechnology, Alma Mater Studiorum, University of Bologna, 40126 Bologna, Italy
[3]MCD, Centre de Biologie Intégrative (CBI), Université de Toulouse, CNRS, UPS, 31062 Toulouse, France
[4]BigA Core Facility, Centre de Biologie Intégrative (CBI), Université de Toulouse, 31062 Toulouse, France
[5]These authors contributed equally
[6]These authors contributed equally
[7]Lead contact
*Correspondence: giovanni.capranico@unibo.it (G.C.), olivier.sordet@inserm.fr (O.S.)
https://doi.org/10.1016/j.celrep.2024.114214

SUMMARY

TDP1 removes transcription-blocking topoisomerase I cleavage complexes (TOP1ccs), and its inactivating H493R mutation causes the neurodegenerative syndrome SCAN1. However, the molecular mechanism underlying the SCAN1 phenotype is unclear. Here, we generate human SCAN1 cell models using CRISPR-Cas9 and show that they accumulate TOP1ccs along with changes in gene expression and genomic distribution of R-loops. SCAN1 cells also accumulate transcriptional DNA double-strand breaks (DSBs) specifically in the G1 cell population due to increased DSB formation and lack of repair, both resulting from abortive removal of transcription-blocking TOP1ccs. Deficient TDP1 activity causes increased DSB production, and the presence of mutated TDP1 protein hampers DSB repair by a TDP2-dependent backup pathway. This study provides powerful models to study TDP1 functions under physiological and pathological conditions and unravels that a gain of function of the mutated TDP1 protein, which prevents DSB repair, rather than a loss of TDP1 activity itself, could contribute to SCAN1 pathogenesis.

INTRODUCTION

Accumulation of DNA breaks in post-mitotic neurons has been associated with multiple neurodegenerative syndromes.[1–4] DNA breaks can accumulate as a result of increased break production and/or inability to repair. A key step in the repair of DNA breaks is the processing of DNA ends to make them suitable for gap filling and ligation. Mutations in several enzymes that process DNA ends underlie neurodegenerative and neurodevelopmental diseases.[1,3] A leading example is the autosomal recessive mutation of tyrosyl DNA phosphodiesterase 1 (TDP1), which causes the neurodegenerative syndrome spinocerebellar ataxia with axonal neuropathy 1 (SCAN1).[5,6] TDP1 processes a broad spectrum of DNA lesions, especially 3′-blocking lesions, both in the nucleus and in mitochondria.[7–12] However, its neuroprotective function seems primarily related to the processing of 3′-topoisomerase I cleavage complexes (TOP1ccs), which are the preferred substrate of TDP1.[11,13]

TOP1ccs are TOP1-linked single-strand breaks (SSBs) that form transiently as TOP1 relaxes DNA during transcription.[14–16] After DNA relaxation, TOP1ccs self-reverse, resulting in TOP1 release from chromatin. However, transient TOP1ccs can be "trapped" under physiological conditions by multiple DNA alterations, giving rise to long-lived TOP1ccs.[14,15] TOP1ccs are also selectively trapped by camptothecins (CPTs),[17] which temporarily prevent the TOP1 re-ligation reaction. Trapped TOP1ccs can block the transcribing RNA polymerase II (Pol II), making the TOP1ccs irreversible.[18–22] TDP1 is the primary enzyme involved in the removal of irreversible transcription-blocking TOP1ccs.[11,23,24] Following partial degradation of a TOP1cc by the ubiquitin/proteasome system, TDP1 cleaves the phosphodiester bond between the TOP1 peptide and the DNA in a two-step catalytic reaction.[18,25–28] First, TDP1 excises the TOP1 peptide from DNA while forming a TDP1-DNA intermediate, called TDP1cc. Then, TDP1cc self-reverses using its H493 residue, resulting in TDP1 release from chromatin. Following TDP1 action, a TOP1-free SSB is generated, which is resealed by the concerted action of polynucleotide kinase 3′-phosphatase (PNKP), X-ray repair cross-complementing group 1 (XRCC1), and DNA ligase III (LIG3).

Transcription-blocking TOP1ccs can lead to the accumulation and genomic redistribution of R-loops,[29–31] structures composed of an RNA/DNA hybrid and a displaced single-strand DNA, and to the formation of DNA double-strand breaks (DSBs).[31–33] Mechanistically, these DSBs can arise from two nearby SSBs on opposing DNA strands, both generated during transcription. One SSB is produced during the removal of a transcription-blocking TOP1cc by the TDP1 pathway, while the other results from the nuclease-mediated cleavage of an R-loop.[31,32] These transcription-dependent DSBs can form in non-replicating cells and trigger cell death.[31–34]

Homozygous *TDP1* H493R mutation causes SCAN1 syndrome.[5,6] Cells derived from SCAN1 patients show an approximately 100-fold reduction in TDP1 activity due to the combined effect of decreased enzyme activity and protein level of mutant TDP1.[23,35] Consistent with the role of H493 residue in TDP1 removal from chromatin, SCAN1 cells accumulate TDP1ccs.[10,35,36] These cells also accumulate TOP1ccs,[24] suggesting that the SCAN1 mutation also affects the first step of TDP1 catalysis. Despite the knowledge on TDP1 biology, it remains unclear whether SCAN1 is caused by a reduction of TDP1 activity, an accumulation of TOP1ccs or TDP1ccs, or a combination of these events.

A major limitation in elucidating the molecular basis of SCAN1 disease is the availability of SCAN1 models. *TDP1* knockout (KO) models do not allow to dissociate the consequences of TDP1 protein loss from the partial activity of mutated TDP1, while cells from SCAN1 patients are not isogenic and only allow comparison of SCAN1 patients with healthy members from the same family. To overcome these limitations, we generate human SCAN1 cells with the same genetic background as parental cells using CRISPR-Cas9 and characterize their phenotype compared to *TDP1* KO cells. We show that SCAN1 cells accumulate transcriptional DSBs due to increased DSB formation and lack of repair. Increased DSB production results from deficient TDP1 activity, whereas defective DSB repair is due to the presence of mutated TDP1 protein, which hampers the action of a TDP2-dependent backup pathway. This points to a gain of function of the mutated TDP1 protein, rather than a loss of activity of TDP1 itself, as responsible for the defective repair of transcriptional DSBs in SCAN1 cells. Our study thereby provides a valuable cellular system and insight into the mechanisms of SCAN1 pathogenesis.

RESULTS

Generation and validation of human SCAN1 cells

To generate SCAN1 cells bearing the same genetic background as parental cells, we edited human U2OS cells using the CRISPR-Cas9 technology to introduce in *TDP1* genes the A1478G mutation found in SCAN1 patients,[5] resulting in TDP1 H493R mutated protein (Figure 1A). We obtained two clones, SCAN1$^{\#1}$ and SCAN1$^{\#2}$, showing complete A1478G conversion (Figure 1B), indicating that the mutation is homozygous. To further test for homozygosity, we exploited that the mutation creates a cleavage site by the BsaAI enzyme. PCR products surrounding the mutation were entirely cleaved by BsaAI in SCAN1 clones (Figure 1C), indicating that both *TDP1* alleles carry the mutation.

SCAN1 U2OS cells showed an approximately 2.5-fold decrease in TDP1 protein expression (Figure 1D), which is consistent with reports in SCAN1 patient cells.[35,37] SCAN1 mutation decreased preferentially *TDP1* mRNA level compared to pre-mRNA level (Figure 1E), suggesting that a decrease in *TDP1* transcript stability rather than in *TDP1* transcription could account for the decreased expression of TDP1 protein in SCAN1. However, these variations of TDP1 protein level did not affect the cell cycle, determined by quantitative image-based cytometry (QIBC) (Figure S1), a high-content automated microscopy technique for assessing cell-cycle distribution at the single-cell level.[31,38–40] SCAN1 U2OS cells also displayed an accumulation of endogenous TOP1ccs (Figure 1F), in agreement with a previous report in SCAN1 patient cells.[24] Thus, SCAN1 U2OS cells recapitulate key features of SCAN1 patient cells, confirming their robustness to study the molecular mechanism underlying SCAN1 pathogenesis.

SCAN1 cells exhibit altered gene expression profiles and R-loop redistribution at specific loci

High levels of TOP1ccs can inhibit global transcription, affect gene expression,[19,32,41,42] and induce R-loops both globally and at specific genes.[29–31,43–46] Therefore, we tested whether the SCAN1 mutation, which increases TOP1cc levels (Figure 1F), affects gene expression and R-loop homeostasis.

Global nascent transcription, assessed by 5-ethynyl uridine (EU) incorporation into newly synthesized RNA, was only slightly decreased in SCAN1 cells (Figures 2A and 2B). Next, we analyzed gene expression by RNA sequencing (RNA-seq). Principal-component analysis (PCA) showed a greater similarity between the two SCAN1 clones than between SCAN1 clones and parental cells (wild-type [WT]) (Figure S2A). Differential expression analyses identified many altered genes in both SCAN1 clones (Figures 2C and 2D; Table S1). In particular, 934 and 1,204 genes were upregulated in SCAN1$^{\#1}$ and SCAN1$^{\#2}$ vs. WT, respectively, and 697 and 962 were downregulated (Figures 2C and 2D; Table S1), with a high reproducibility between biological replicates (Figure S2B). In agreement with mRNA and protein analyses (Figures 1D and 1E), RNA-seq data confirmed a 2- to 2.4-fold reduction of *TDP1* transcripts in SCAN1 cells (Figure S2C). The overall gene expression changes were significantly conserved between the two SCAN1 clones (Figure S2D), suggesting that major changes are not related to clonal selection. Consistently, many genes showing changes in expression were found in both SCAN1 clones (705 upregulated and 418 downregulated; Figure 2D). Gene set over-representation analysis (GSOA) of genes upregulated in both SCAN1 clones showed a low but significant enrichment in terms of extracellular matrix (ECM) organization and collagen formation in the Reactome analysis (Figure 2E) and ECM- and collagen-related terms in the Gene Ontology (GO) analysis (Figure S2E). Thus, SCAN1 mutation induces an alteration of gene expression, particularly genes involved in ECM-related pathways, without major changes in the expression of genes related to nuclear processes and in overall nascent transcription.

R-loop homeostasis was investigated by assessing global level of nuclear R-loops by slot blot with the S9.6 antibody, which recognizes RNA/DNA hybrids.[47,48] S9.6 signal increased in

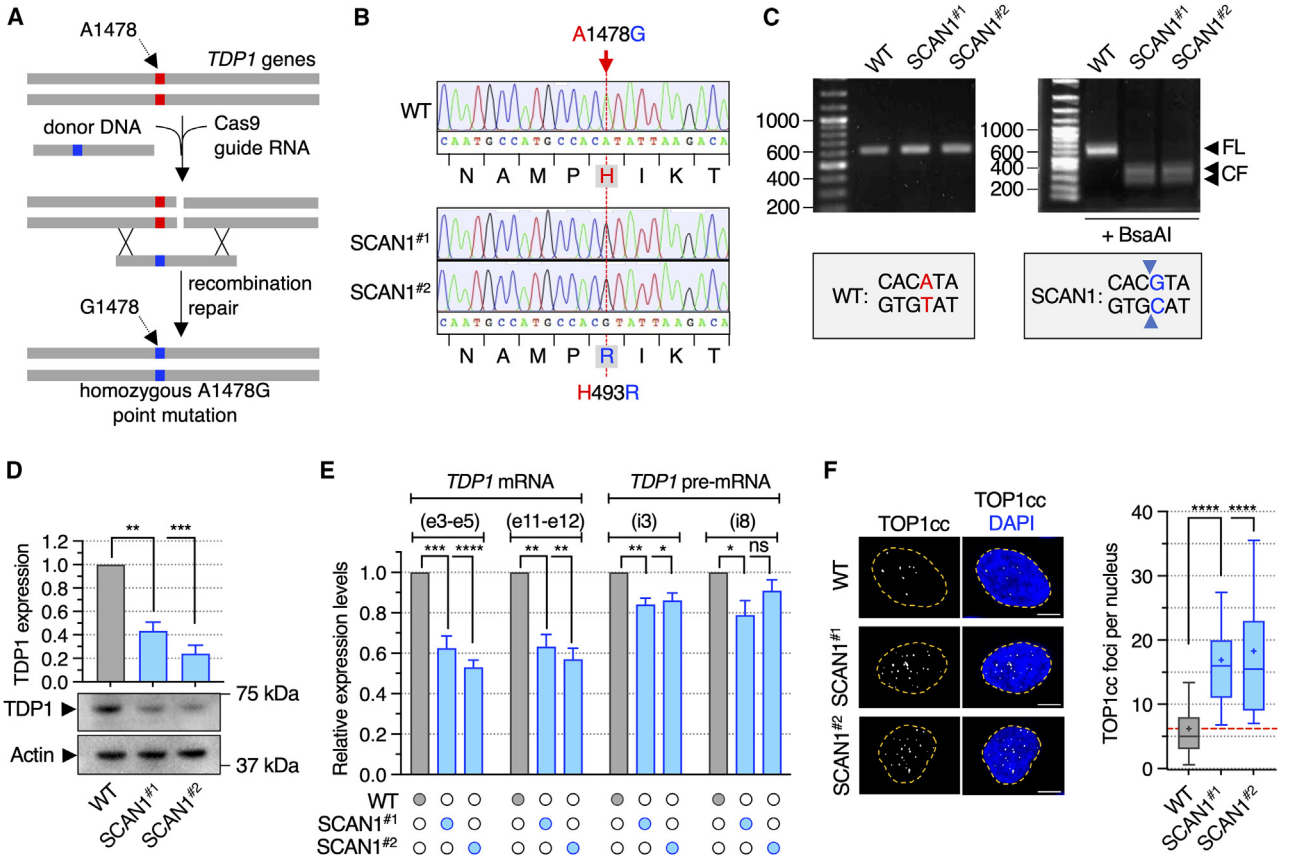

Figure 1. Generation and characterization of U2OS cells with homozygous *TDP1* H493R mutation

(A) Scheme for generation of homozygous point mutation in *TDP1* genes.

(B) DNA sequencing showing introduction of SCAN1 mutation in two clones from U2OS cells.

(C) Agarose gel of DNA PCR fragments from *TDP1* WT and SCAN1 cells exposed to BsaAI enzyme. FL, full length; CF, cleaved fragment.

(D) Western blot of TDP1 in *TDP1* WT and SCAN1 cells. Actin, loading control. Top: quantification of TDP1 normalized to actin (means ± SEM; $n = 3$). $^{**}p < 0.01$, $^{***}p < 0.001$ (two-tailed unpaired t test).

(E) qRT-PCR of *TDP1* transcripts in *TDP1* WT and SCAN1 cells (means ± SEM; $n \geq 3$). ns, not significant; $^{*}p < 0.05$, $^{**}p < 0.01$, $^{***}p < 0.001$, $^{****}p < 0.0001$ (two-tailed unpaired t test). e, exon; i, intron.

(F) *TDP1* WT and SCAN1 cells were stained for TOP1ccs. Left: representative images. Scale bars: 5 μm. Right: number of TOP1cc foci per nucleus in a representative experiment out of ≥3. $^{****}p < 0.0001$ (two-tailed unpaired t test). See also Figure S1.

SCAN1 cells compared to WT cells (Figure 2F), suggesting that the SCAN1 mutation causes an overall R-loop increase in the nucleus. RNase H treatment suppressed S9.6 signal, confirming its specificity for RNA/DNA hybrids (Figure 2F). To assess the overall level of R-loops in the nucleoplasm where the majority of Pol II transcription takes place, we used immunofluorescence (IF) microscopy and quantified the nuclear S9.6 signal after subtracting the nucleolar signal, as described.[44,49,50] SCAN1 cells showed no significant increase in S9.6 signal in the nucleoplasm (Figure 2G), suggesting that the global increase in the nucleus (Figure 2F) is likely due to an increase of R-loops in the nucleolus rather than in Pol II-transcribed genes. Therefore, we examined whether this unchanged S9.6 nucleoplasmic signal was related to unchanged R-loop level or to concurrent R-loop increases and decreases at Pol II-transcribed genes. To address this, we performed RNA/DNA hybrid immunoprecipitation (DRIP)-seq with the S9.6 antibody. We detected an average of 85,995 DRIP peaks in WT cells and 87,100 peaks in SCAN1$^{\#1}$ cells between the DRIP-seq replicates. Among them, 51,744 and 53,595 DRIP peaks mapped on annotated genes in WT and SCAN1$^{\#1}$, respectively. Thus, SCAN1 cells display a similar DRIP-peak number and genic distribution. As R-loop signal has been positively correlated with gene expression,[51] we analyzed the relationship between R-loop signal and SCAN1-gene expression changes identified by RNA-seq (Figures 2C and 2D). Both SCAN1 clones showed a preferential increase and decrease in DRIP signal at genes that were respectively upregulated and downregulated compared to WT cells (Figures 2H and S3A). Representative single-gene results for *ZNF114* and *CD70*, genes upregulated in both SCAN1 clones, exemplified the increased DRIP signal in SCAN1 cells compared to WT cells (Figures 2I, S3B and S3C). Genes with unchanged expression level between WT and SCAN1 cells (non-REG) showed no preferential change in R-loop signal (Figures 2H and S3A). This

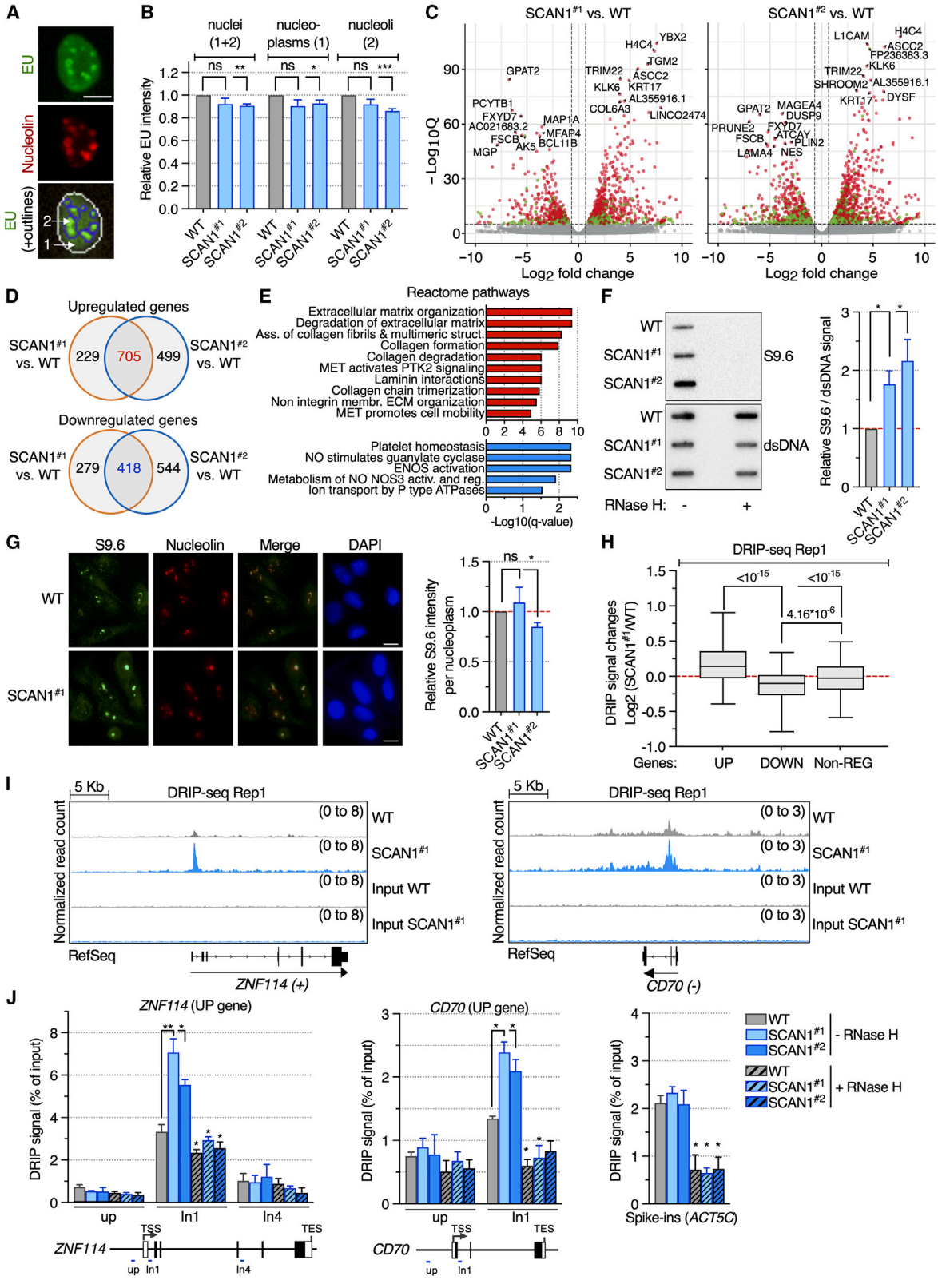

(legend on next page)

resulted from the concurrent presence of non-REG genes displaying increased, decreased, or unchanged R-loop signal, as shown for the *NPM1* and *TUFT1* non-REG genes presenting increased and unchanged DRIP signal, respectively (Figures S3D and S3F). DRIP-seq data were confirmed by gene-specific DRIP-qPCR carried out in presence of *Drosophila* spike-ins controls (Figures 2J, S3E, and S3G). RNase H treatment reduced the DRIP signal in DRIP-qPCR thus, confirming R-loop specificity (Figures 2J, S3E, and S3G). Next, we asked whether R-loops accumulate over preferential genic regions in SCAN1-upregulated genes. DRIP signal was increased throughout the gene region, from transcription start site (TSS) to transcription end site (TES), with the most significant enrichment in the TSS-proximal genic region (TSS to TSS + 2 kb vs. TSS + 2 kb to TES) in both SCAN1 clones (Figures S3H–S3J). Together, these results suggest that increased R-loop levels at specific loci could be correlated, at least on SCAN1 upregulated genes, to their increased expression.

Overall, the results from transcriptomic and R-loop analyses indicate altered gene expression and R-loop redistribution at specific Pol II-transcribed genes in SCAN1 cells, which is consistent with elevated levels of TOP1ccs.

SCAN1 cells accumulate transcriptional DSBs due to increased DSB production

Another consequence of high levels of TOP1ccs is the production of DSBs, which can be replication dependent[52,53] and/or transcription dependent.[31–33] Therefore, we tested whether SCAN1 cells accumulate DSBs by analyzing nuclear foci of γH2AX (phosphorylated H2AX at S139). SCAN1 U2OS cells are cycling and thus, to assess the influence of transcription and replication on DSBs, γH2AX was analyzed distinctly in the G1, S, and G2 phases of the cell cycle. Cells were analyzed by QIBC,[31,38,39] which allows simultaneous assessment of cell-cycle distribution and γH2AX foci counting at the single-cell level. SCAN1 cells showed an increased number of γH2AX foci specifically in the G1 phase (Figures 3A and S4A–S4C). Consistently, the number of p53BP1 foci (phosphorylated 53BP1 at S1778) was also increased in G1 (Figure S4D). In line with SCAN1 cells showing no increased DSBs in S and G2 phases (Figures 3A and S4A–S4C), they also showed no increase in the number of micronuclei (Figure 3B), which can form when cells with unrepaired DSBs go through mitosis.[54] These results indicate that SCAN1 cells accumulate DSBs selectively in the G1 phase, suggesting that these breaks may originate from transcription.

The increase in γH2AX and p53BP1 due to the SCAN1 mutation is robust but relatively modest (Figures 3A and S4A–S4D). Therefore, we monitored DSBs upon exposure to CPT, which amplifies TOP1cc-dependent phenotypes by the rapid and selective induction of high levels of TOP1ccs.[17,23,24,31–33,35,36] Consistent with TOP1ccs causing G1-specific accumulation of DSBs in SCAN1 cells (Figures 3A and S4A–S4D), a short CPT treatment also increased γH2AX selectively in G1 (Figures 3C and S4C) compared to S phase (Figures S4C and S4E-G). γH2AX increase in G1 was suppressed by the Pol II inhibitor 5,6-dichlorobenzimidazole 1-β-D-ribofuranoside (DRB) (Figure 3C), indicating that DSBs depend on transcription. CPT-induced transcriptional DSBs can originate from SSB intermediates generated downstream of TOP1 degradation during the removal of transcription-blocking TOP1ccs by the TDP1 pathway.[31,32] Hence, we inhibited TOP1cc degradation with the proteasome inhibitor MG132 to prevent the generation of these SSB intermediates, as reported.[31,32] MG132 prevented CPT-induced γH2AX foci in SCAN1 cells (Figure 3C), suggesting that SSB intermediates generated during TOP1cc removal are involved in DSB production. TOP1 proteolysis in SCAN1 cells was similar to WT cells in response to CPT (Figure S4H), excluding that changes in TOP1 proteolysis could account for higher DSBs in SCAN1 cells. By contrast to G1, γH2AX induction in S phase was not markedly affected in SCAN1 cells compared to WT cells (Figures S4C and S4E–S4G) and was not prevented by DRB and only partially by MG132 (Figures S4E and S4F). This is in agreement with CPT primarily inducing replication-dependent DSBs in S phase,[52,53] which depend partially on TOP1 degradation at arrested replication forks.[55] Intriguingly, CPT induced a DRB- and MG132-dependent increase of γH2AX in SCAN1 cells in G2 (Figure S4I), suggesting an increased production of transcriptional DSBs in G2. However, in contrast to G1, SCAN1 cells did not accumulate DSBs in G2 (Figures 3A and S4A–S4C). This suggests that DSB accumulation in G1 may

Figure 2. Mutated TDP1 affects gene expression and R-loop genomic distribution

(A and B) *TDP1* WT and SCAN1 cells were incubated with EU (1 mM; 30 min) before staining for EU, nucleolin, and Hoechst. (A) Representative images. White line, nucleus; blue lines, nucleoli; arrows, nucleoplasm (1) and nucleoli (2). Scale bar: 10 μm. (B) EU intensity normalized to *TDP1* WT cells (means ± SEM; $n = 4$). ns, not significant; $^{*}p < 0.05$, $^{**}p < 0.01$, $^{***}p < 0.001$ (two-tailed unpaired t test).

(C) Volcano plot of differential expression analysis for SCAN1 vs. *TDP1* WT cells. Green dots, genes exceeding thresholds for fold change (x axis, 1.5) and q value (y axis, 10e−5). Red dots, genes exceeding the above-mentioned thresholds in both clones. The 10 most upregulated and downregulated genes are labeled.

(D) Venn diagram of common genes upregulated (top) and downregulated (bottom) in SCAN1 vs. *TDP1* WT cells.

(E) GSOA of upregulated (red) and downregulated (blue) genes in both SCAN1 clones tested on Reactome pathways. Bar heights indicate –log10(q value) of overrepresentation test.

(F) RNA/DNA hybrid slot blot of genomic DNA ± RNase H from *TDP1* WT and SCAN1 cells. Left: representative slot blot. dsDNA, loading control. Right: values are normalized to dsDNA (means ± SEM; $n = 5$). $^{*}p < 0.05$ (two-tailed unpaired t test).

(G) *TDP1* WT and SCAN1 cells were stained for S9.6, nucleolin, and DAPI. Left: representative images. Scale bar: 10 μm. Right: S9.6 intensity per nucleoplasm normalized to *TDP1* WT cells (means ± SEM; $n = 4$). ns, not significant; $^{*}p < 0.05$ (two-tailed unpaired t test).

(H) Boxplots showing DRIP-seq signal changes in SCAN1$^{\#1}$ cells, log2 (SCAN1$^{\#1}$/WT), of genes that are upregulated (UP), downregulated (DOWN), or non-regulated (Non-REG) in both SCAN1 clones compared to *TDP1* WT cells in RNA-seq. Numbers are *p* values (unpaired Mann-Whitney test).

(I and J) DRIP analysis of *ZNF114* and *CD70* UP genes in *TDP1* WT and SCAN1 cells. (I) DRIP-seq profiles. Numbers in brackets indicate normalized read counts.

(J) DRIP-qPCR analysis ± exogenous RNase H. The *Drosophila ACT5C* gene is used as spike-ins. Values represent percentage of input (means ± SEM; $n = 3$). $^{*}p < 0.05$, $^{**}p < 0.01$ (two-tailed paired t test). Gene diagrams with primer position used are shown at bottom. Rep1, replicate 1. See also Figures S2 and S3.

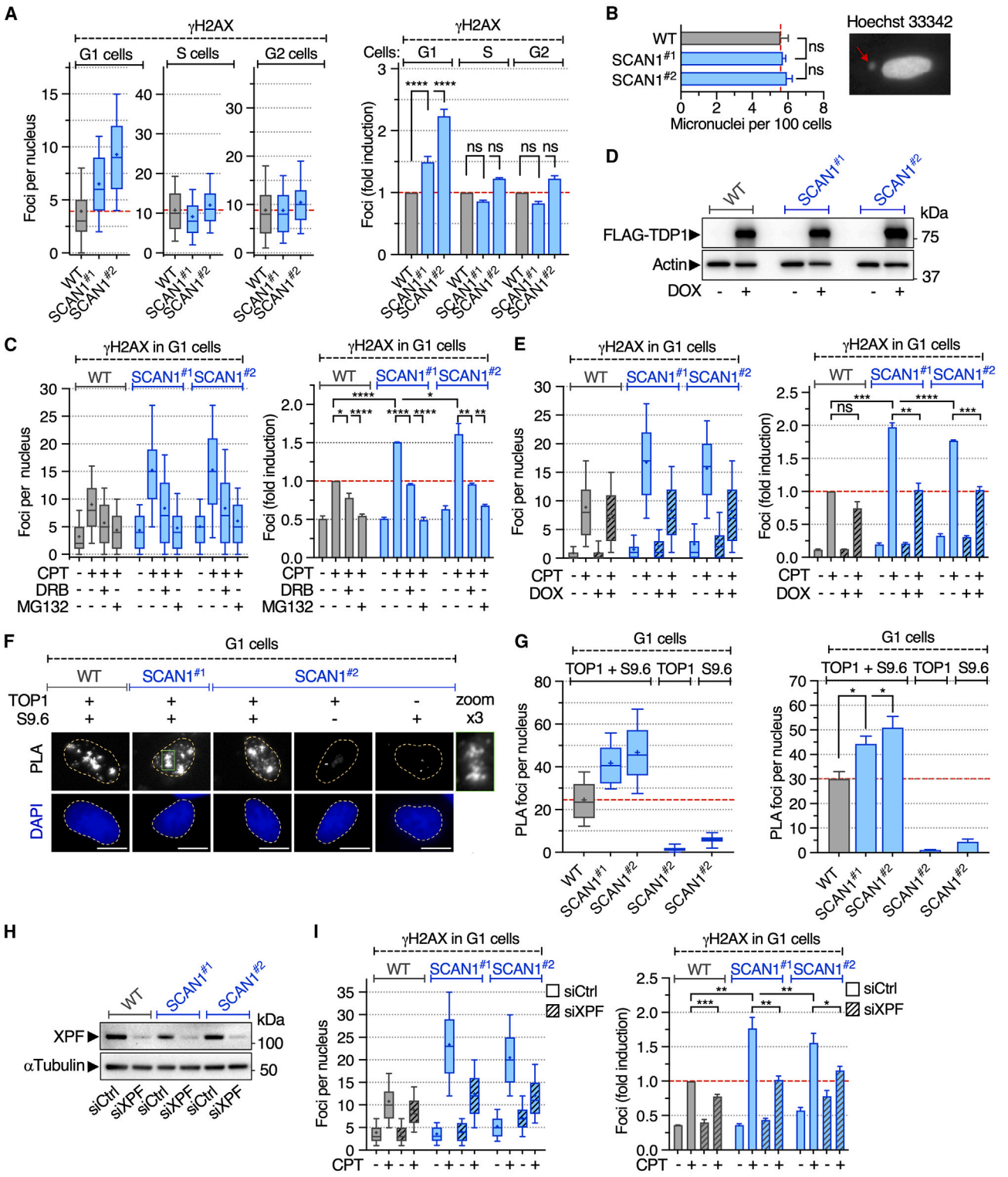

Figure 3. Mutated TDP1 promotes accumulation of transcriptional DSBs in G1 cells due to increased DSB production

(A) *TDP1* WT and SCAN1 cells were incubated with 5-ethynyl-2'-deoxyuridine (EdU) (10 μM; 30 min) before staining for EdU, γH2AX, and Hoechst. Left: number of γH2AX foci per G1, S, and G2 nucleus. Right: fold induction of γH2AX foci normalized to *TDP1* WT cells (means ± SEM; $n = 5$). ns, not significant; ****$p < 0.0001$ (one-way ANOVA).

(B) Number of micronuclei per 100 cells (means ± SEM; $n = 6$). ns, not significant (two-tailed paired t test). Red arrow shows a micronucleus.

(legend continued on next page)

not simply result from increased DSB production. To control that the G1-specific increase of DSBs was strictly caused by the *TDP1* mutation, we engineered SCAN1 cells to induce TDP1 WT upon doxycycline treatment (Figure 3D). Expression of TDP1 WT fully reversed the SCAN1-dependent induction of γH2AX by CPT in G1 (Figure 3E).

The production of transcriptional DSBs induced by TOP1ccs depends on R-loops,[31,33] and SCAN1 cells displayed changes in R-loop genomic distribution (Figures 2H–2J and S3). We therefore investigated whether R-loops are involved in the G1-specific accumulation of DSBs in SCAN1 cells. We first tested TOP1cc enrichment at R-loops by proximity ligation assay (PLA) using TOP1 and S9.6 antibodies to visualize the close proximity of TOP1 and RNA/DNA hybrids at chromatin. The number of PLA foci increased in SCAN1 cells specifically in G1 (Figures 3F and 3G) compared to S phase (Figure S4J), suggesting a G1-specific increase of TOP1cc and R-loop proximity. To assess the direct consequences of R-loops, we prevented their cleavage, which is necessary for the production of TOP1cc-induced transcriptional DSBs in quiescent cells.[31] Depletion of xeroderma pigmentosum complementation group F (XPF), one of the endonucleases responsible for R-loop cleavage,[31,49,56] suppressed the SCAN1-dependent increase of γH2AX by CPT specifically in G1 (Figures 3H and 3I) compared to S phase (Figure S4K).

Together, these results suggest that increased R-loop-dependent DSB production, resulting from abortive removal of transcription-blocking TOP1ccs, contributes to accumulation of transcriptional DSBs in SCAN1 cells in G1 phase.

SCAN1 cells accumulate transcriptional DSBs due to defective DSB repair

Next, we assessed whether DSB accumulation in SCAN1 cells also depends on defective DSB repair. To that end, we analyzed the reversal kinetics of CPT-induced γH2AX and p53BP1 foci after drug wash-out, as reported.[31,57] In *TDP1* WT G1 cells, the number of γH2AX and p53BP1 foci decreased rapidly after CPT removal (Figures 4A–4D). By contrast, SCAN1 mutation suppressed the reversal of γH2AX and p53BP1 (Figures 4A–4D), indicating defective DSB repair. Analysis of S-phase cells showed that the SCAN1 mutation did not affect the reversal kinetics of γH2AX (Figure 4E), which is consistent with the lack of DSB accumulation in SCAN1 cells in S phase (Figures 3A and S4A–S4C).

These results point to an essential role of TDP1 in the repair of transcriptional DSBs. TDP1 may promote non-homologous end-joining (NHEJ),[58–61] a prevalent pathway for DSB repair in G0/G1.[62] Alternatively, given the nature of TOP1cc-induced transcriptional DSBs that are formed by two separate SSBs,[31] TDP1 could promote DSB repair by repairing TOP1-linked SSBs. To test these possibilities, we used quiescent WI38-hTERT cells treated with CPT, which allow the specific and unique induction of transcriptional DSBs.[31,32]

Depletion of two key NHEJ factors with small interfering RNAs (siRNAs), XRCC4 or LIG4, did not affect the reversal kinetics of p53BP1 foci after CPT removal in quiescent cells (Figures S5), suggesting that TOP1cc-induced transcriptional DSBs are not repaired by NHEJ. Therefore, we tested whether TDP1 could promote DSB repair by repairing TOP1-linked SSBs. TDP1 forms a complex with PNKP, XRCC1, LIG3α, and poly-(ADP-ribose) polymerase 1 (PARP1) (Figure 5A). Following TDP1 action, a protein-free SSB is generated, which is processed by PNKP before ligation by LIG3α-XRCC1.[11,12] PARP1 promotes the recruitment of TDP1 along with XRCC1 at TOP1cc sites.[63] Depletion of each component of this pathway with siRNAs (i.e., PARP1, PNKP, XRCC1, LIG3; Figure 5B) and TDP1[31] delayed the reversal of p53BP1 foci after CPT removal in quiescent cells (Figures 5C–5F).[31] Similar results were obtained in U2OS cells in G1 (Figures 5G and 5H), indicating that TOP1cc-induced transcriptional DSBs are repaired by the TDP1-mediated SSB repair pathway, and all the proteins of the TDP1 complex (Figure 5A) participate in it. Therefore, these findings can mechanistically explain the inability of SCAN1 cells to repair transcriptional DSBs.

SCAN1-mutated TDP1 hampers the repair of transcriptional DSBs by a TDP2-dependent backup pathway

In contrast to SCAN1 mutation, which completely prevents the repair of transcriptional DSBs (Figure 4), siRNA-mediated depletion of TDP1 pathway components only delays it (Figure 5).[31] Although this may be related to the partial knockdown of proteins by siRNAs, another possibility is that the absence of TDP1 is mechanistically different from the presence of the SCAN1 mutated TDP1 protein in the repair of transcriptional DSBs. To investigate this, we generated *TDP1* KO cells by CRISPR-Cas9 in U2OS (Figures 6A and S6A) and compared them with SCAN1 cells.

(C) *TDP1* WT and SCAN1 cells were incubated with EdU (10 μM) ± DRB (50 μM) or MG132 (10 μM) for 1 h before the addition of CPT (25 μM) for 1 h while maintaining EdU, EdU/DRB, or EdU/MG312 in the media. Cells were then stained for EdU, γH2AX, and Hoechst. Left: number of γH2AX foci per G1 nucleus. Right: γH2AX foci in G1 nuclei normalized to CPT-treated *TDP1* WT cells (means ± SEM; $n = 3$). *$p < 0.05$, **$p < 0.01$, ****$p < 0.0001$ (two-tailed unpaired t test).
(D and E) *TDP1* WT and SCAN1 FLAG-TDP1 cells were induced with doxycycline (DOX) to express FLAG-TDP1. (D) Western blot of FLAG-TDP1. Actin, loading control. (E) Cells were incubated with EdU (10 μM; 30 min) before the addition of CPT (25 μM; 1 h) and stained for EdU, γH2AX, and Hoechst. Left: number of γH2AX foci per G1 nucleus. Right: γH2AX foci in G1 nuclei normalized to CPT-treated *TDP1* WT cells (means ± SEM; $n = 3$). ns, not significant; **$p < 0.01$, ***$p < 0.001$, ****$p < 0.0001$ (two-tailed unpaired t test).
(F and G) *TDP1* WT and SCAN1 cells were incubated with EdU (10 μM; 30 min) and stained for EdU, DAPI, and PLA between TOP1 and S9.6 antibodies. (F) Representative images of G1 cells. Dashed lines indicate nuclei. Scale bars: 10 μm. Zoom shows that individual foci can also be counted in foci-dense regions. (G) Number of PLA foci in the whole nucleus of G1 cells in a representative experiment (left) and three independent experiments (right: means ± SEM; $n = 3$). *$p < 0.05$ (two-tailed unpaired t test). Single-antibody controls from SCAN1$^{\#2}$ cells are shown.
(H and I) *TDP1* WT and SCAN1 cells were transfected with siRNAs against XPF or a firefly luciferase control sequence (siCtrl). (H) Western blot of XPF. αTubulin, loading control. (I) Cells were incubated with EdU (10 μM; 30 min) before the addition of CPT (5 μM; 1 h) and stained for EdU, γH2AX, and Hoechst. Left: number of γH2AX foci per G1 nucleus. Right: γH2AX foci in G1 nuclei normalized to CPT-treated *TDP1* WT cells (means ± SEM; $n = 4$). *$p < 0.05$, **$p < 0.01$, ***$p < 0.001$ (two-tailed unpaired t test). A representative experiment out of five (A; left), three (C, E, G; left), or four (I; left) is shown. See also Figure S4.

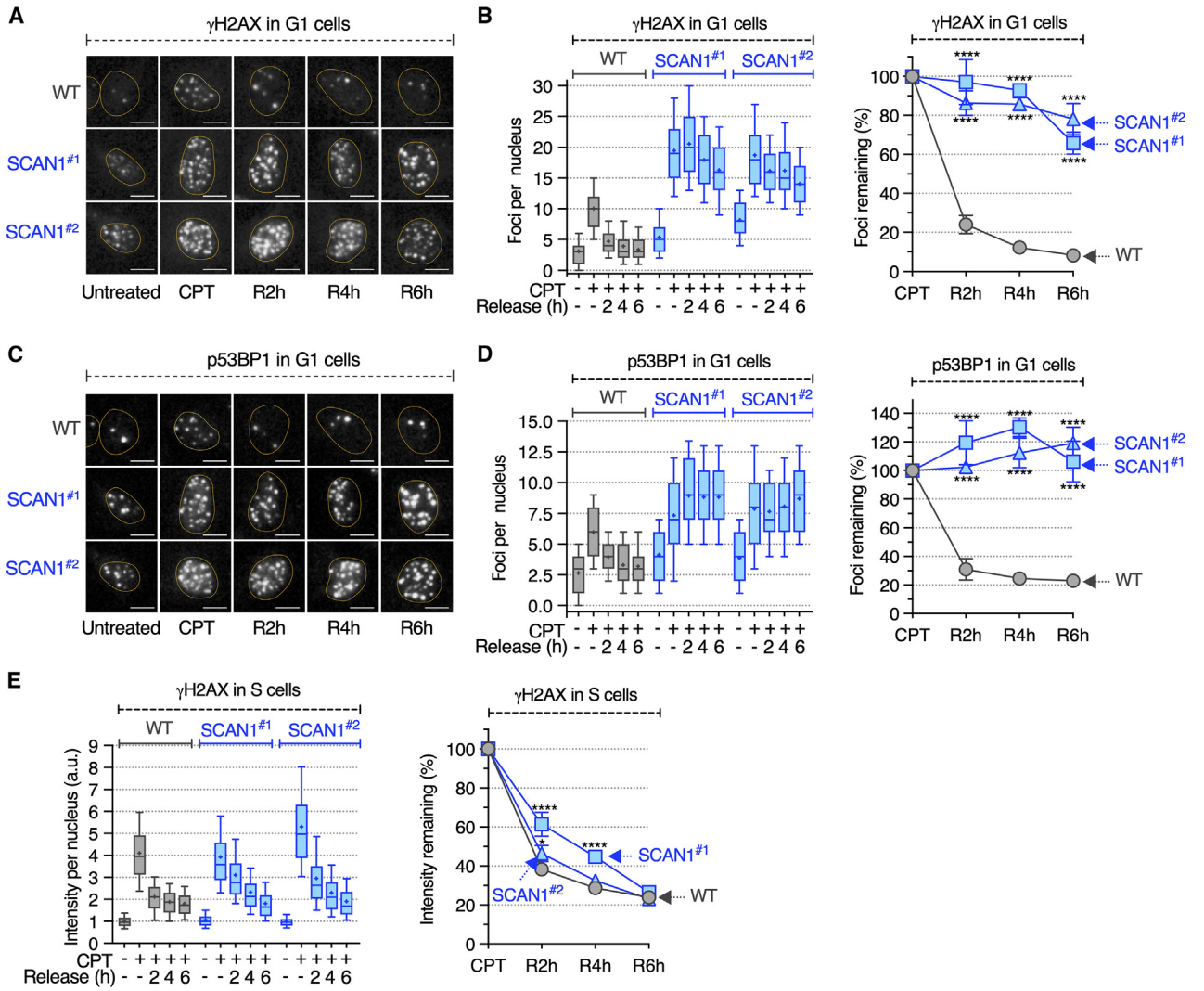

Figure 4. Mutated TDP1 prevents the repair of transcriptional DSBs in G1 cells

TDP1 WT and SCAN1 cells were incubated with EdU (10 μM; 30 min) before the addition of CPT (25 μM; 1 h), washed, and cultured in CPT-free medium (R, release) containing EdU (10 μM) for up to 6 h. Cells were then stained for EdU, γH2AX, p53BP1, and Hoechst.

(A and B) Analysis of γH2AX foci in G1 cells. (A) Representative images. Yellow lines indicate nuclei. Scale bars: 10 μm. (B) Left: number of γH2AX foci per G1 nucleus. Right: percentages of γH2AX foci remaining in G1 nuclei following CPT removal normalized to CPT-treated cells (means ± SEM; $n \geq 3$). ****$p < 0.0001$ (mixed-effects analysis, Tukey's multiple comparisons test).

(C and D) Analysis of p53BP1 foci in G1 cells as in (A) and (B).

(E) Analysis of γH2AX intensity in S cells as in (B). Right: means ± SEM; $n \geq 3$. *$p < 0.05$, ****$p < 0.0001$ (mixed-effects analysis, Tukey's multiple comparisons test).

A representative experiment out of four (B, D, E; left) is shown.

As for SCAN1 cells (Figures 1, 2, 3, and 4), *TDP1* KO cells displayed an increase of endogenous TOP1ccs (Figures 6B and S6B), R-loops (Figures 6C and S6C), and γH2AX specifically in G1 phase (Figures 6D, S6D and S6E). In response to CPT, *TDP1* KO further showed that TOP1 proteolysis (Figure S6F) and a G1-specific increase of γH2AX (Figure 6E) were similar to SCAN1 cells, suggesting that TDP1 loss of expression mimics the SCAN1 mutation in the production of transcriptional DSBs. Similar to cells depleted for TDP1 with siRNAs (Figures 5G and 5H),[31] *TDP1* KO cells showed a delay in DSB repair compared to WT cells specifically in G1 (Figures 6E and S6G) compared to S phase (Figure S6H). However, unlike SCAN1 cells that did not repair DSBs in G1 (Figures 4A–4D, 6E, and S6G), *TDP1* KO cells could ultimately repair them (Figures 6E and S6G). Expression of all components of the TDP1 repair complex was maintained in SCAN1 and *TDP1* KO cells (Figures 6F and S7A), as reported in SCAN1 patient cells,[23] excluding that depletion of proteins of the TDP1 complex could account for the differences in DSB repair between these cells.

The ultimate repair of transcriptional DSBs in *TDP1* KO but not in SCAN1 cells could be due to a compensatory mechanism in absence of TDP1 but not in presence of mutated TDP1 protein.

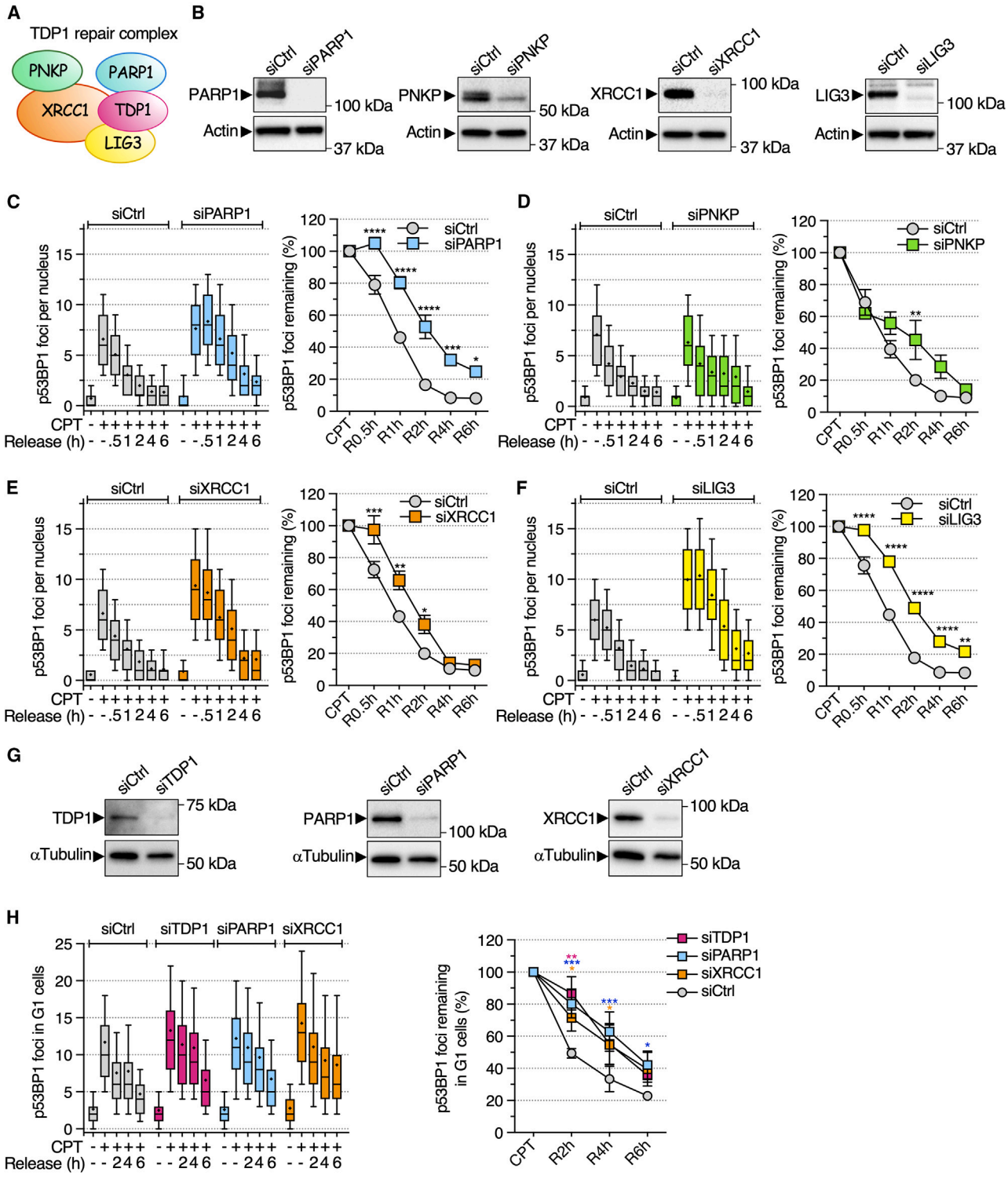

Figure 5. Depletion of components of the TDP1 repair complex delays the repair of transcriptional DSBs in quiescent and G1 cells

(A) Representation of the TDP1 repair complex.

(B–F) Quiescent WI38-hTERT cells were transfected with the indicated siRNAs. (B) Western blot probed with the indicated antibodies. Actin, loading control. (C–F) Cells were treated with CPT (25 μM; 1 h), washed, and cultured in CPT-free medium (R, release) for up to 6 h. Cells were then stained for p53BP1 and Hoechst and analyzed for the number of p53BP1 foci per nucleus. Left: representative experiment out of three (C, D, and E) or four (F). Right: percentages of p53BP1 foci

(legend continued on next page)

TDP2 can repair TOP1ccs in absence of TDP1,[64,65] and, therefore, we tested the potential role of TDP2 in the repair of transcriptional DSBs in *TDP1* KO cells compared to SCAN1 cells. First, TDP2 expression increased in *TDP1* KO and SCAN1 cells (Figures S7A and S7B), linking TDP2 expression to impaired TDP1 activity. Next, we depleted TDP2 with siRNAs in *TDP1* KO, SCAN1, and WT cells (Figure 6G) and analyzed DSB repair upon CPT removal in G1. TDP2 depletion in *TDP1* KO cells led to persistent p53BP1 and γH2AX foci after CPT removal to the same extent as the SCAN1 mutation (Figures 6G, S7C, and S7D). By contrast, TDP2 depletion did not affect repair kinetics in *TDP1* WT cells (Figures 6G, S7C, and S7D).

To investigate the mechanism by which TDP2 compensates for the loss of TDP1 but not for mutated TDP1 protein in the repair of transcriptional DSBs, we tested whether TDP2 is part of the TDP1 repair complex (Figure 5A) in absence of TDP1 but not in presence of mutated TDP1. To do this, we performed co-immunoprecipitation (coIP) experiments in HEK293T cells transfected with plasmids expressing TDP2 and components of the complex (XRCC1, LIG3α, PNKP) in presence or absence of TDP1 (WT or H493R). IP of XRCC1 pulled down the whole complex but not TDP2 in cells expressing TDP1 WT or TDP1 mutant (Figure 6H). This suggests that, in SCAN1 cells, TDP1 mutant is part of the complex, as reported,[23] and that TDP2 is not. In absence of TDP1, XRCC1 was also able to pull down the complex but was not able to co-immunoprecipitate TDP2 (Figure 6H). As TDP1 interacts directly with LIG3α in the complex,[23,66] we then asked whether, in cells lacking TDP1, the absence of TDP2 in the complex could be related to the inability of TDP2 to interact with LIG3α. Bioluminescence resonance energy transfer (BRET) experiments showed that LIG3α interacted with both TDP1 WT and TDP1 mutant but not with TDP2 (Figure 6I). BRET competition experiments further confirmed the specificity of LIG3α/TDP1 WT and LIG3α/TDP1 mutant interactions and showed that TDP2 did not affect these protein-protein interactions (Figures 6J, S7E, and S7F). Together, these experiments indicate that TDP2 compensates for the loss of TDP1 in the repair of transcriptional DSBs without being recruited to the complex as a surrogate component.

We therefore asked whether TDP2-mediated repair of transcriptional DSBs in *TDP1* KO cells still requires the action of the repair complex downstream to TDP2 action. To address this, we depleted XRCC1 in *TDP1* KO, SCAN1, and WT cells and analyzed DSB repair upon CPT removal in G1. Similar to TDP2 depletion (Figures 6G, S7C, and S7D), XRCC1 depletion in *TDP1* KO cells led to persistent p53BP1 and γH2AX foci after CPT removal (Figures 6K, S7G, and S7H), suggesting that, even though TDP2 is not part of the complex, they both act in the same pathway for the repair of transcriptional DSBs.

To get further insight into the mechanism by which mutated TDP1 hampers TDP2 action in repairing transcriptional DSBs, we depleted mutated TDP1 with siRNAs in SCAN1 cells (Figure 7A). This resulted in the ability of cells to reverse p53BP1 foci upon CPT removal in G1 (Figure 7B). By contrast, concurrent depletion of TDP1 and TDP2 led back to defective repair in SCAN1 cells (Figures 7A and 7B). Taken together, these results indicate that the presence of mutated TDP1 hampers the repair of transcriptional DSBs, likely by preventing TDP2 action, pointing to a gain of function of the mutated TDP1 protein, rather than a loss of activity of TDP1 itself, as responsible for the defective repair of transcriptional DSBs in SCAN1 cells.

DISCUSSION

SCAN1 is caused by the homozygous TDP1 H493R mutation,[5] but it is unclear how this mutation initiates SCAN1 pathology. The main limitation to study SCAN1 is the availability of models, which are restricted to cells from patients.[5] Other models consist of ectopic expression of mutated TDP1 into *TDP1*-deficient human[10] and yeast cells.[67,68] Here, we generate a human model of SCAN1 cells with the same genetic background as parental cells, and we show that SCAN1 cells display elevated TOP1cc levels, altered gene expression, genomic redistribution of R-loops, and accumulation of transcriptional DSBs due to both increased DSB production and defective repair. Mechanistically, a TDP2-mediated compensatory pathway can repair DSBs in absence of TDP1 but not in presence of mutated TDP1 H493R protein.

Our findings reveal that SCAN1 cells accumulate TOP1ccs, which have been reported to affect gene expression[19,32,41,42] and R-loop homeostasis.[29–31,43–46] In line with these TOP1cc-associated phenotypes, SCAN1 cells display altered gene expression, including changes in pathways related to ECM and basal lamina components, which have been connected with neurodegenerative diseases.[69,70] Trapped TOP1ccs represent a barrier to the elongating Pol II,[18,21,22] and hence an early response to CPT is a global inhibition of transcription.[25,32] However, genes are differentially affected, with a fraction of them, primarily the short and low-expressed genes, being upregulated.[41,42,71] CPT-induced trapped TOP1ccs may increase gene expression indirectly, such as by enhancing transcription initiation and enhancer RNA (eRNA) transcription.[42,72] This could explain why SCAN1 cells display an overall, albeit modest, decrease in transcription but also the upregulation of some genes. We showed that R-loops are redistributed in SCAN1 cells, with genes showing increased R-loop level being preferentially upregulated genes. Hence, this suggests a correlation between R-loop level and transcriptional changes in SCAN1 cells, which is in agreement with R-loops being positively correlated with gene expression.[51] However, some genes that are not upregulated also display increased R-loop level, suggesting that other mechanisms besides gene expression might be involved in R-loop redistribution in SCAN1 cells. For instance, physical Pol II blockade by trapped TOP1ccs could promote R-loop formation (Figure 7C) by displacing the

remaining following CPT removal normalized to CPT-treated cells; means ± SEM; $n = 3$ (C, D, and E) or 4 (F). $^{*}p < 0.05$, $^{**}p < 0.01$, $^{***}p < 0.001$, $^{****}p < 0.0001$ (two-way ANOVA).

(G and H) U2OS cells were transfected with the indicated siRNAs. (G) Western blot probed with the indicated antibodies. αTubulin, loading control. (H) Cells were incubated with EdU (10 μM; 30 min) before treatment, staining, and analysis as in (C)–(F). Means ± SEM; $n = 3$; $^{*}p < 0.05$, $^{**}p < 0.01$, $^{***}p < 0.001$ (two-way ANOVA). See also Figure S5.

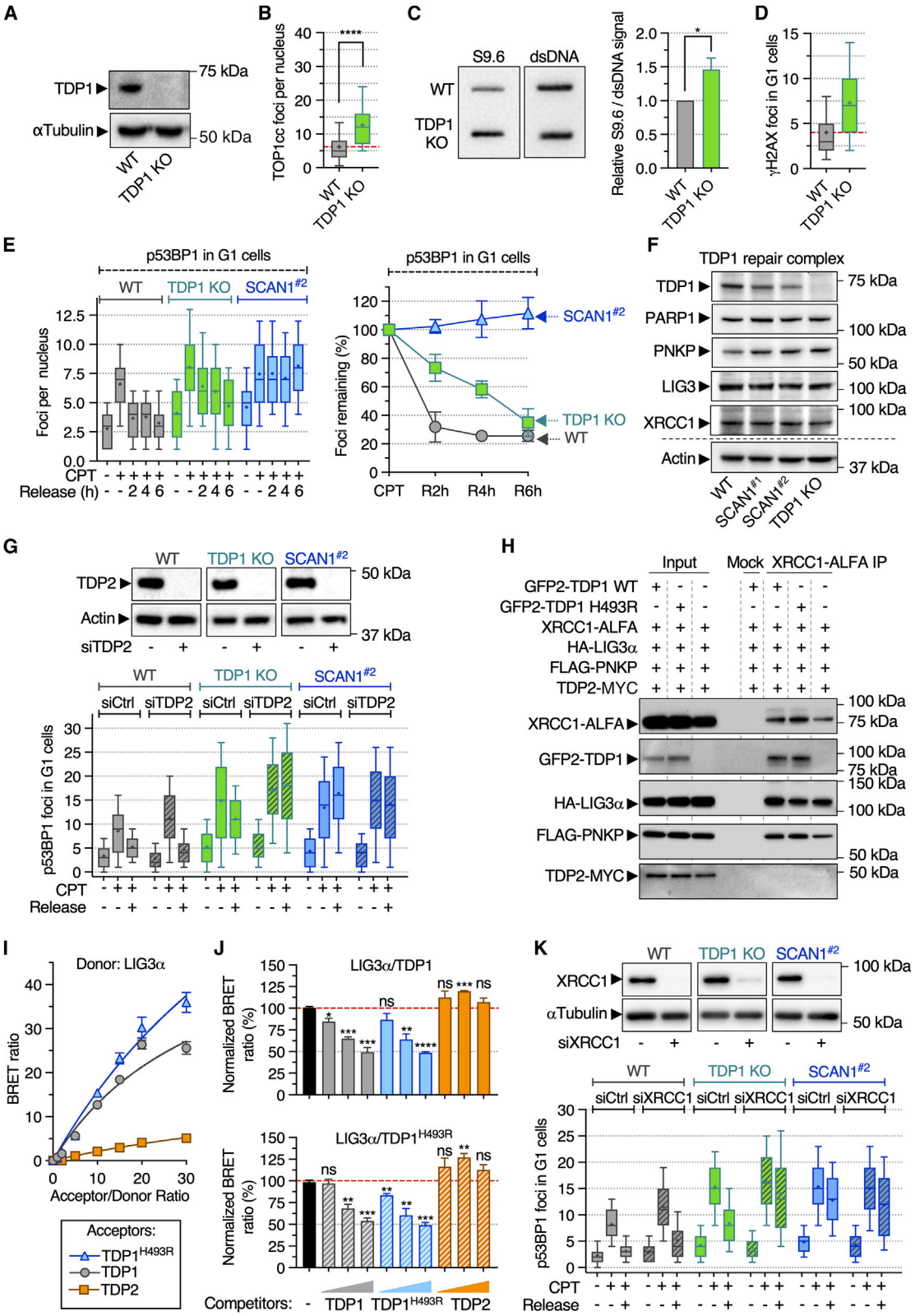

(legend on next page)

spliceosome.[73] Alternatively, enhanced TOP1cc trapping in SCAN1 cells could lead to decreased TOP1 activity, which in turn could promote R-loop formation because of accumulation of negative supercoiling[74] and/or interference with splicing.[75,76] In line with this possibility, CPT decreases TOP1 activity[17] and TOP1 depletion triggers R-loop redistribution.[77,78] These concurrent R-loop increases and decreases over distinct genic regions could result in a global unchanged R-loop level at Pol II-transcribed genes, as we measured in the nucleoplasm. Hence, the increase in global R-loop signal detected by slot blot in SCAN1 cells may possibly reflect increased R-loop level at ribosomal DNA (rDNA), albeit mitochondrial R-loop signal due to contamination during nuclei isolation cannot be completely excluded. The increased R-loop level at rDNA genes is in agreement with a well-established function of TOP1 in maintaining R-loop homeostasis at these genes in both yeast and human cells[77,79] and the potential role of stabilized TOP1ccs in triggering increased R-loop level at rDNA.[29,80]

SCAN1 patient cells display drastic reduction in TDP1 activity due to both decreased catalytic activity and protein level of mutated TDP1.[23,35] Decreased protein level could result from its enhanced ubiquitylation and degradation due to downregulation of the deubiquitylase UCHL3, as shown in SCAN1 patient cells,[37] and/or from decreased transcript stability (this study), which could be related to changed *TDP1* mRNA sequence as a result of the mutation.[81] Because of the very low activity of mutated TDP1, it was suggested that SCAN1 disease may result from a loss of function of TDP1.[5] However, our findings reveal that SCAN1 cells differ from *TDP1* KO cells in their ability to handle transcriptional DSBs in G1 phase, pointing to a gain of function of the mutated TDP1 protein, rather than a loss of function of TDP1 itself, as responsible for the defective repair of transcriptional DSBs in SCAN1 cells. The possibility that a gain of function of mutant TDP1 could underlie SCAN1 neurodegenerative phenotype is in line with several studies showing that TDP1 depletion in mice,[36,82,83] flies,[84,85] and zebrafish[86] results in only moderate or no neurodegeneration.

Our data indicate that transcriptional DSBs in SCAN1 and *TDP1* KO cells can arise from two nearby SSBs on opposing DNA strands, one being produced by a transcription-blocking TOP1cc peptide and the second by R-loop cleavage (Figure 7C), as we previously described in non-replicating cells.[31] Production of transcriptional DSBs requires XPF-mediated R-loop cleavage in CPT-treated quiescent cells,[31] and XPF has been reported to cleave R-loops in several other contexts.[49,56,87] However, we cannot exclude that XPF-mediated cleavage of other structures than R-loops[88] could also be involved in XPF-dependent production of transcriptional DSBs in CPT-treated SCAN1 cells in G1 phase. According to our model (Figure 7C), SCAN1 and *TDP1* KO cells would display DSBs with 3′-broken DNA strands attached to TOP1 peptides, which need to be cleansed to allow DSB repair. Our data showing that TDP2 promotes the repair of transcriptional DSBs in *TDP1* KO cells therefore suggest that TDP2 can remove TOP1ccs in absence of TDP1, which is consistent with other independent studies.[64,65] However, TDP1 and TDP2 exhibit little structural or sequence similarity,[89] which may explain why, unlike TDP1,[23,66] TDP2 does not bind to LIG3α and is not recruited to the TDP1 repair complex in absence of TDP1. Nevertheless, although TDP2 is not part of the complex, it requires it to repair transcriptional DSBs. This is consistent with TDP2 having, albeit weak, a 3′-tyrosyl DNA phosphodiesterase activity similar to TDP1,[90] leading to a TOP1-free SSB that would be resealed by the concerted action of PNKP/XRCC1/LIG3α. Thus, our work raises the question of why TDP2 does not remove TOP1ccs in SCAN1 cells to repair transcriptional DSBs. As mutated TDP1 is part of the complex (this study and El-Khamisy et al.[23]) but with very low activity,[23,35] it is possible that the complex remains stalled on TOP1ccs, physically hindering their access to TDP2.

Our findings point toward a repair of transcriptional DSBs relying on the repair of two SSBs rather than on the repair of the DSB itself by DSB repair pathways. This non-canonical mechanism of DSB repair may be related to the nature of these transcriptional DSBs, which are formed by two SSBs on opposing DNA strands.[31] The lack of DSB accumulation in S and G2 phases

Figure 6. TDP2 compensates TDP1 loss for the repair of transcriptional DSBs

(A) Western blot of TDP1 in *TDP1* WT and KO U2OS cells. αTubulin, loading control.

(B) Number of TOP1cc foci per nucleus in *TDP1* WT and KO cells. ****$p < 0.0001$ (two-tailed unpaired t test). Data with *TDP1* WT cells are from the same experiment as in Figure 1F.

(C) RNA/DNA hybrid slot blot of genomic DNA from *TDP1* WT and KO cells. Left: representative slot blot. dsDNA, loading control. Right: values are normalized to dsDNA (means ± SEM; $n = 5$). *$p < 0.05$ (two-tailed unpaired t test). Quantification data with *TDP1* WT cells are from the same experiment as in Figure 2F.

(D) *TDP1* WT and KO cells were incubated with EdU (10 μM; 30 min) before staining for EdU, γH2AX, and Hoechst. The number of γH2AX foci per G1 nucleus is shown.

(E) *TDP1* WT, KO, and SCAN1 cells were incubated with EdU (10 μM; 30 min) before the addition of CPT (25 μM; 1 h), washed, and cultured in CPT-free medium (R, release) containing EdU (10 μM) for up to 6 h. Cells were then stained for EdU, p53BP1, and Hoechst. Left: number of p53BP1 foci per G1 nucleus. Right: percentages of p53BP1 foci remaining in G1 nuclei following CPT removal normalized to CPT-treated cells (means ± SEM; $n = 3$).

(F) Western blot probed with the indicated antibodies in *TDP1* WT, SCAN1, and KO cells. Actin, loading control.

(G) *TDP1* WT, KO, and SCAN1 cells were transfected with siCtrl (−) or siTDP2 (+). Top: western blot of TDP2. Actin, loading control. Bottom: cells were treated as in (E) with 10 μM CPT and a release of 8 h. The number of p53BP1 foci per G1 nucleus is shown.

(H) Cell extracts from HEK293T cells transfected with the indicated plasmids were immunoprecipitated with nanobody ALFA-coupled agarose beads (XRCC1-ALFA IP). IP and input fractions were analyzed by western blotting with the indicated anti-tag antibody.

(I) BRET donor saturation assay between LIG3α (donor) and TDP1, $TDP1^{H493R}$ or TDP2 (acceptors) (means ± SD of quadruplicates).

(J) BRET competition assays between LIG3α/TDP1 (top) or LIG3α/$TDP1^{H493R}$ (bottom) interactions and TDP1, $TDP1^{H493R}$, and TDP2 used as competitors (means ± SD; $n = 3$). ns, not significant; *$p < 0.05$, **$p < 0.01$, ***$p < 0.001$, ****$p < 0.0001$ (two-tailed unpaired t test).

(K) Same experiment as in (G) with siXRCC1 transfection. A representative experiment out of four (B, F, and G bottom), five (C left, D), three (E left, I, K bottom), and two (H) is shown. See also Figures S6 and S7.

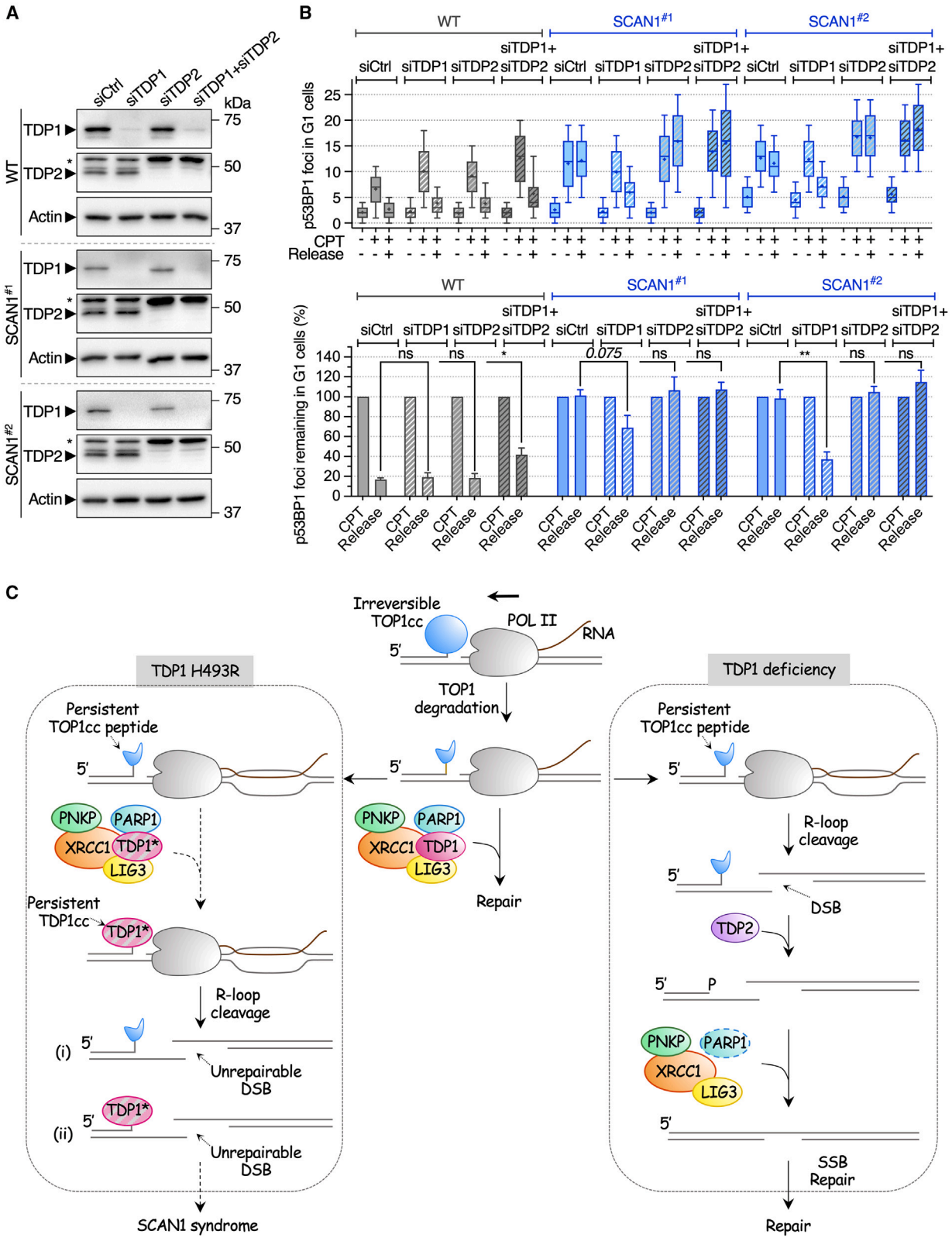

(legend on next page)

further suggests that transcriptional DSBs could be repaired by homologous recombination (HR), which is available in S and G2, but not in G1 due to absence of sister chromatids for recombination. This scenario is further supported by the increased production of transcriptional DSBs in G2 phase of SCAN1 cells, which does not result in DSB accumulation. Therefore, it is plausible that transcriptional DSBs formed in SCAN1 cells in G0/G1 may be repaired in S phase. This possibility is in line, from a molecular point of view, with increased HR in SCAN1 cells,[23] and, from a clinical point of view, with SCAN1 syndrome primarily affecting non-replicating cells. Hence, these cells could accumulate unrepaired transcriptional DSBs as they do not enter S phase.

The accumulation of transcriptional DSBs due to SCAN1 mutation is relatively modest, which could be consistent with SCAN1 syndrome appearing late in the teenage years.[5,6] Therefore, it is conceivable that these persistent DSBs could accumulate over time in neurons of SCAN1 patients, contributing to the neurodegenerative phenotype. This could be due to a direct DSB-mediated activation of cell death, as reported in non-replicating cells.[31,32] Alternatively, DNA damage could affect ECM remodeling,[91] thus indirectly affecting survival and apoptotic pathways. Both scenarios point to a possible contribution of unrepairable transcriptional DSBs in neurodegeneration. A further connection between defective TOP1cc repair, transcriptional DSBs, and neurodegeneration comes from other genetic defects in the TOP1cc repair pathway, such as in *PNKP* and *XRCC1*, which enhance transcriptional DSBs in non-replicating cells (this study and Cristini et al.[31]) and underlie neurodegenerative diseases.[1,3,4,92,93] In addition, several genetic defects causing R-loop deregulation, such as in *SETX*, *RNASEH2*, *C9orf72*, *SMN*, *FXN*, and *FMR1* genes, also underlie neurodegenerative diseases.[4,46,87,94–97] Neurons may be particularly prone to accumulate transcriptional DSBs because of high rates of oxygen consumption, which produces reactive oxygen species that can trap TOP1ccs[11,98] and induce other 3′-DNA blocking lesions, such as 3′-phosphoglycolate and 3′-abasic site, all requiring TDP1 for processing.[9,99,100] Consistently, oxidative stress has been implicated in several neurodegenerative diseases.[101] It has been recently reported that SCAN1 cells also display mitochondrial dysfunction, which could further contribute to the SCAN1 phenotype.[10]

In summary, our study provides robust models to study SCAN1 syndrome at the molecular level, allowing key physiological roles of TDP1 in gene expression, R-loop homeostasis, and prevention of transcriptional DSBs in G0/G1 cells to be unraveled. Furthermore, these results uncover a potential function of TDP1 H493R mutated protein in the accumulation of unrepairable DSBs thus, providing insight into the molecular mechanisms of SCAN1 pathogenesis.

Limitations of the study

A potential limitation is the use of U2OS cells when investigating a neurodegenerative disease. We chose these cells because they are widely used for both gene editing and DNA damage-associated applications. This model cannot assess the SCAN1 mutation's impact on DNA damage in the context of post-mitotic (G0) cells, but nonetheless allows us to study it in the absence of replication in G1. It also aids in understanding why SCAN1 syndrome does not affect replicating cells.

Although SCAN1 cells can accumulate both TOP1ccs and TDP1ccs, we did not investigate TDP1ccs because their detection is not straightforward. Mutated TDP1 is only weakly expressed and, unlike TOP1ccs, there are currently no antibodies available against TDP1ccs.

PLA experiments assessed proximity between TOP1ccs and R-loops in both nucleoplasm and nucleoli. Because the anti-RNA/DNA hybrid S9.6 antibody can recognize ribosomal RNA,[102,103] some PLA foci originating from nucleoli, possibly the zoomed-in "dense regions," may not be specific to TOP1cc and RNA/DNA hybrid colocalization.

STAR★METHODS

Detailed methods are provided in the online version of this paper and include the following:

- KEY RESOURCES TABLE
- RESOURCE AVAILABILITY
  - Lead contact
  - Materials availability
  - Data and code availability
- EXPERIMENTAL MODEL AND STUDY PARTICIPANT DETAILS
  - Cells and treatments
- METHOD DETAILS
  - Generation of U2OS cells *TDP1* H493R (SCAN1) and *TDP1* KO
  - Molecular cloning
  - Generation of U2OS cells inducible for 3xFLAG-TDP1
  - Cell extracts and immunoblotting
  - RNA analysis by qRT-PCR
  - Immunofluorescence microscopy of TOP1cc
  - Quantification of global nascent RNA transcription
  - RNA-seq and data analyses
  - RNA/DNA hybrid slot blot

Figure 7. Depletion of mutated TDP1 restores the repair of transcriptional DSBs

(A and B) *TDP1* WT and SCAN1 cells were transfected with the indicated siRNAs. (A) Western blot of TDP1 and TDP2. Asterisk (*) indicates non-specific band. Actin, loading control. (B) Cells were incubated with EdU (10 μM; 30 min) before the addition of CPT (10 μM; 1 h), washed, and cultured in CPT-free medium (Release) containing EdU (10 μM) for 8 h. Cells were then stained for EdU, p53BP1, and Hoechst. Top: number of p53BP1 foci per G1 nucleus. Bottom: percentages of p53BP1 foci remaining in G1 nuclei following CPT removal normalized to CPT-treated cells (means ± SEM; $n = 3$). ns, not significant; $^{*}p < 0.05$, $^{**}p < 0.01$ (two-tailed unpaired t test).

(C) Model for accumulation of transcriptional DSBs in SCAN1 cells. A transcription-blocking TOP1cc is proteolyzed by the proteasome leading to a TOP1 peptide-linked SSB. TDP1, which is part of a complex containing PARP1/PNKP/LIG3/XRCC1, excises the TOP1 peptide, allowing the repair of the TOP1-SSB lesion. Right: TDP1 loss leads to the persistence of the TOP1 peptide-linked SSB, which favors R-loop formation and its cleavage by endonucleases leading to a DSB, as reported.[31] TDP2 excises the TOP1 peptide, generating a TOP1-free SSB that is repaired by PNKP/LIG3/XRCC1. SSB repair on opposing DNA strand leads to DSB repair. Left: mutated TDP1 (TDP1*) decreases TDP1 activity, leading to the persistence of a TOP1 peptide-linked SSB and a TDP1(H493R)-linked SSB, which favor R-loop formation and DSBs harboring a 3′-TOP1 peptide end (i) or a 3′-TDP1(H493R) end (ii). These DNA ends hamper DSB repair, leading to DSB accumulation, which could contribute to SCAN1 phenotype.

SUPPLEMENTAL INFORMATION

Supplemental information can be found online at https://doi.org/10.1016/j.celrep.2024.114214.

ACKNOWLEDGMENTS

We thank Yvan Canitrot, Jérémie Fages, and Guillaume Labrousse for help with the CRISPR-Cas9 experimental setup to generate SCAN1 cells; Carl Mann for WI38-hTERT cells; Luisa Di Stefano for *Drosophila* S2 cells; the CRCT Platform and Laetitia Ligat for technical assistance in microscopy and for generating Fiji macro for TOP1cc analysis; and Jakob Freudenberger for help in DRIP-qPCR. The O.S. lab is supported by INSERM, the Fondation pour la Recherche Médicale (FRM) (équipe labellisée FRM [DEQ20170839117]), and the Institut National Du Cancer (INCA_16730). Research activity in the G.C. lab is supported by AIRC (Associazione Italiana per la Ricerca sul Cancro, Milan, Italy) (IG 2019, ID: 23032 project, PI Capranico Giovanni) and the Ministry of University and Research under PRIN 2017 (KSZZJW_004 project, PI Marinello Jessica). The D.T. lab is supported by a grant from the Ligue Nationale Contre le Cancer (LNCC, as an équipe labellisée). E.N. holds a tenured research position from the INSERM (France). M.G. is supported by fellowships from the Agence Régionale de Santé Occitanie, the Fondation ARC, and the Institut National Du Cancer (INCA_16730); A.C. from the Fondation de France (engagements: 00097702, 00113878, and 00119148); S.S. from the French-Italian University VINCI Program; N.B. from the Fondation de France (engagements: 00097692, 00112961, and 00119146); and A.C.A. and L.F.M. from the LNCC (CAR/IP/SC-17551 for A.C.A.; IP/SC/SK-17250 for L.F.M.).

AUTHOR CONTRIBUTIONS

M.G., A.C., S.S., N.B., A.C.A., L.F.M., and O.S. designed, performed, and analyzed the experiments. V.J. and M.R. performed bioinformatics analyses of DRIP-seq and RNA-seq, respectively. J.M., P.C., D.T., G.F., E.N., and G.C. contributed to data analysis. G.C. and O.S. conceived the study. O.S. supervised the study. A.C. and O.S. wrote the manuscript with contributions from the other authors.

DECLARATION OF INTERESTS

The authors declare no competing interests.

Received: March 2, 2023
Revised: March 5, 2024
Accepted: April 24, 2024
Published: May 17, 2024

REFERENCES

1. Caldecott, K.W. (2022). DNA single-strand break repair and human genetic disease. Trends Cell Biol. *32*, 733–745. https://doi.org/10.1016/j.tcb.2022.04.010.
2. Rass, U., Ahel, I., and West, S.C. (2007). Defective DNA repair and neurodegenerative disease. Cell *130*, 991–1004. https://doi.org/10.1016/j.cell.2007.08.043.
3. Jiang, B., Glover, J.N.M., and Weinfeld, M. (2017). Neurological disorders associated with DNA strand-break processing enzymes. Mech. Ageing Dev. *161*, 130–140. https://doi.org/10.1016/j.mad.2016.07.009.
4. Cristini, A., Gromak, N., and Sordet, O. (2020). Transcription-dependent DNA double-strand breaks and human disease. Mol. Cell. Oncol. *7*, 1691905. https://doi.org/10.1080/23723556.2019.1691905.
5. Takashima, H., Boerkoel, C.F., John, J., Saifi, G.M., Salih, M.A.M., Armstrong, D., Mao, Y., Quiocho, F.A., Roa, B.B., Nakagawa, M., et al. (2002). Mutation of TDP1, encoding a topoisomerase I-dependent DNA damage repair enzyme, in spinocerebellar ataxia with axonal neuropathy. Nat. Genet. *32*, 267–272. https://doi.org/10.1038/ng987.
6. Salih, M.A.M., Takashima, H., and Boerkoel, C.F. (1993). Spinocerebellar Ataxia with Axonal Neuropathy Type 1. In GeneReviews((R)), M.P. Adam, J. Feldman, G.M. Mirzaa, R.A. Pagon, S.E. Wallace, L.J.H. Bean, K.W. Gripp, and A. Amemiya, eds.
7. Das, B.B., Dexheimer, T.S., Maddali, K., and Pommier, Y. (2010). Role of tyrosyl-DNA phosphodiesterase (TDP1) in mitochondria. Proc. Natl. Acad. Sci. USA *107*, 19790–19795. https://doi.org/10.1073/pnas.1009814107.
8. Yang, S.W., Burgin, A.B., Jr., Huizenga, B.N., Robertson, C.A., Yao, K.C., and Nash, H.A. (1996). A eukaryotic enzyme that can disjoin dead-end covalent complexes between DNA and type I topoisomerases. Proc. Natl. Acad. Sci. USA *93*, 11534–11539. https://doi.org/10.1073/pnas.93.21.11534.
9. Interthal, H., Chen, H.J., and Champoux, J.J. (2005). Human Tdp1 cleaves a broad spectrum of substrates, including phosphoamide linkages. J. Biol. Chem. *280*, 36518–36528. https://doi.org/10.1074/jbc.M508898200.
10. Ghosh, A., Bhattacharjee, S., Chowdhuri, S.P., Mallick, A., Rehman, I., Basu, S., and Das, B.B. (2019). SCAN1-TDP1 trapping on mitochondrial DNA promotes mitochondrial dysfunction and mitophagy. Sci. Adv. *5*, eaax9778. https://doi.org/10.1126/sciadv.aax9778.
11. Pommier, Y., Huang, S.y.N., Gao, R., Das, B.B., Murai, J., and Marchand, C. (2014). Tyrosyl-DNA-phosphodiesterases (TDP1 and TDP2). DNA Repair *19*, 114–129. https://doi.org/10.1016/j.dnarep.2014.03.020.
12. Zagnoli-Vieira, G., and Caldecott, K.W. (2020). Untangling trapped topoisomerases with tyrosyl-DNA phosphodiesterases. DNA Repair *94*, 102900. https://doi.org/10.1016/j.dnarep.2020.102900.
13. Katyal, S., Lee, Y., Nitiss, K.C., Downing, S.M., Li, Y., Shimada, M., Zhao, J., Russell, H.R., Petrini, J.H.J., Nitiss, J.L., and McKinnon, P.J. (2014). Aberrant topoisomerase-1 DNA lesions are pathogenic in neurodegenerative genome instability syndromes. Nat. Neurosci. *17*, 813–821. https://doi.org/10.1038/nn.3715.
14. Pommier, Y., Nussenzweig, A., Takeda, S., and Austin, C. (2022). Human topoisomerases and their roles in genome stability and organization. Nat. Rev. Mol. Cell Biol. *23*, 407–427. https://doi.org/10.1038/s41580-022-00452-3.
15. Pommier, Y., Sun, Y., Huang, S.Y.N., and Nitiss, J.L. (2016). Roles of eukaryotic topoisomerases in transcription, replication and genomic stability. Nat. Rev. Mol. Cell Biol. *17*, 703–721. https://doi.org/10.1038/nrm.2016.111.
16. Capranico, G., Marinello, J., and Chillemi, G. (2017). Type I DNA Topoisomerases. J. Med. Chem. *60*, 2169–2192. https://doi.org/10.1021/acs.jmedchem.6b00966.
17. Pommier, Y. (2006). Topoisomerase I inhibitors: camptothecins and beyond. Nat. Rev. Cancer *6*, 789–802. https://doi.org/10.1038/nrc1977.
18. Sordet, O., Larochelle, S., Nicolas, E., Stevens, E.V., Zhang, C., Shokat, K.M., Fisher, R.P., and Pommier, Y. (2008). Hyperphosphorylation of RNA polymerase II in response to topoisomerase I cleavage complexes and its association with transcription- and BRCA1-dependent

degradation of topoisomerase I. J. Mol. Biol. *381*, 540–549. https://doi.org/10.1016/j.jmb.2008.06.028.

19. Capranico, G., Ferri, F., Fogli, M.V., Russo, A., Lotito, L., and Baranello, L. (2007). The effects of camptothecin on RNA polymerase II transcription: roles of DNA topoisomerase I. Biochimie *89*, 482–489. https://doi.org/10.1016/j.biochi.2007.01.001.

20. Baranello, L., Wojtowicz, D., Cui, K., Devaiah, B.N., Chung, H.J., Chan-Salis, K.Y., Guha, R., Wilson, K., Zhang, X., Zhang, H., et al. (2016). RNA Polymerase II Regulates Topoisomerase 1 Activity to Favor Efficient Transcription. Cell *165*, 357–371. https://doi.org/10.1016/j.cell.2016.02.036.

21. Bendixen, C., Thomsen, B., Alsner, J., and Westergaard, O. (1990). Camptothecin-stabilized topoisomerase I-DNA adducts cause premature termination of transcription. Biochemistry *29*, 5613–5619. https://doi.org/10.1021/bi00475a028.

22. Wu, J., and Liu, L.F. (1997). Processing of topoisomerase I cleavable complexes into DNA damage by transcription. Nucleic Acids Res. *25*, 4181–4186. https://doi.org/10.1093/nar/25.21.4181.

23. El-Khamisy, S.F., Saifi, G.M., Weinfeld, M., Johansson, F., Helleday, T., Lupski, J.R., and Caldecott, K.W. (2005). Defective DNA single-strand break repair in spinocerebellar ataxia with axonal neuropathy-1. Nature *434*, 108–113. https://doi.org/10.1038/nature03314.

24. Miao, Z.H., Agama, K., Sordet, O., Povirk, L., Kohn, K.W., and Pommier, Y. (2006). Hereditary ataxia SCAN1 cells are defective for the repair of transcription-dependent topoisomerase I cleavage complexes. DNA Repair *5*, 1489–1494. https://doi.org/10.1016/j.dnarep.2006.07.004.

25. Desai, S.D., Zhang, H., Rodriguez-Bauman, A., Yang, J.M., Wu, X., Gounder, M.K., Rubin, E.H., and Liu, L.F. (2003). Transcription-dependent degradation of topoisomerase I-DNA covalent complexes. Mol. Cell Biol. *23*, 2341–2350. https://doi.org/10.1128/MCB.23.7.2341-2350.2003.

26. Interthal, H., Pouliot, J.J., and Champoux, J.J. (2001). The tyrosyl-DNA phosphodiesterase Tdp1 is a member of the phospholipase D superfamily. Proc. Natl. Acad. Sci. USA *98*, 12009–12014. https://doi.org/10.1073/pnas.211429198.

27. Davies, D.R., Interthal, H., Champoux, J.J., and Hol, W.G.J. (2002). The crystal structure of human tyrosyl-DNA phosphodiesterase. Tdp1. Structure *10*, 237–248. https://doi.org/10.1016/s0969-2126(02)00707-4.

28. Davies, D.R., Interthal, H., Champoux, J.J., and Hol, W.G.J. (2003). Crystal structure of a transition state mimic for Tdp1 assembled from vanadate, DNA, and a topoisomerase I-derived peptide. Chem. Biol. *10*, 139–147. https://doi.org/10.1016/s1074-5521(03)00021-8.

29. Marinello, J., Chillemi, G., Bueno, S., Manzo, S.G., and Capranico, G. (2013). Antisense transcripts enhanced by camptothecin at divergent CpG-island promoters associated with bursts of topoisomerase I-DNA cleavage complex and R-loop formation. Nucleic Acids Res. *41*, 10110–10123. https://doi.org/10.1093/nar/gkt778.

30. Marinello, J., Bertoncini, S., Aloisi, I., Cristini, A., Malagoli Tagliazucchi, G., Forcato, M., Sordet, O., and Capranico, G. (2016). Dynamic Effects of Topoisomerase I Inhibition on R-Loops and Short Transcripts at Active Promoters. PLoS One *11*, e0147053. https://doi.org/10.1371/journal.pone.0147053.

31. Cristini, A., Ricci, G., Britton, S., Salimbeni, S., Huang, S.Y.N., Marinello, J., Calsou, P., Pommier, Y., Favre, G., Capranico, G., et al. (2019). Dual Processing of R-Loops and Topoisomerase I Induces Transcription-Dependent DNA Double-Strand Breaks. Cell Rep. *28*, 3167–3181.e6. https://doi.org/10.1016/j.celrep.2019.08.041.

32. Cristini, A., Park, J.H., Capranico, G., Legube, G., Favre, G., and Sordet, O. (2016). DNA-PK triggers histone ubiquitination and signaling in response to DNA double-strand breaks produced during the repair of transcription-blocking topoisomerase I lesions. Nucleic Acids Res. *44*, 1161–1178. https://doi.org/10.1093/nar/gkv1196.

33. Sordet, O., Redon, C.E., Guirouilh-Barbat, J., Smith, S., Solier, S., Douarre, C., Conti, C., Nakamura, A.J., Das, B.B., Nicolas, E., et al. (2009). Ataxia telangiectasia mutated activation by transcription- and topoisomerase I-induced DNA double-strand breaks. EMBO Rep. *10*, 887–893. https://doi.org/10.1038/embor.2009.97.

34. Cristini, A., Géraud, M., and Sordet, O. (2021). Transcription-associated DNA breaks and cancer: A matter of DNA topology. Int. Rev. Cell Mol. Biol. *364*, 195–240. https://doi.org/10.1016/bs.ircmb.2021.05.001.

35. Interthal, H., Chen, H.J., Kehl-Fie, T.E., Zotzmann, J., Leppard, J.B., and Champoux, J.J. (2005). SCAN1 mutant Tdp1 accumulates the enzyme–DNA intermediate and causes camptothecin hypersensitivity. EMBO J. *24*, 2224–2233. https://doi.org/10.1038/sj.emboj.7600694.

36. Hirano, R., Interthal, H., Huang, C., Nakamura, T., Deguchi, K., Choi, K., Bhattacharjee, M.B., Arimura, K., Umehara, F., Izumo, S., et al. (2007). Spinocerebellar ataxia with axonal neuropathy: consequence of a Tdp1 recessive neomorphic mutation? EMBO J. *26*, 4732–4743. https://doi.org/10.1038/sj.emboj.7601885.

37. Liao, C., Beveridge, R., Hudson, J.J.R., Parker, J.D., Chiang, S.C., Ray, S., Ashour, M.E., Sudbery, I., Dickman, M.J., and El-Khamisy, S.F. (2018). UCHL3 Regulates Topoisomerase-Induced Chromosomal Break Repair by Controlling TDP1 Proteostasis. Cell Rep. *23*, 3352–3365. https://doi.org/10.1016/j.celrep.2018.05.033.

38. Berti, M., Teloni, F., Mijic, S., Ursich, S., Fuchs, J., Palumbieri, M.D., Krietsch, J., Schmid, J.A., Garcin, E.B., Gon, S., et al. (2020). Sequential role of RAD51 paralog complexes in replication fork remodeling and restart. Nat. Commun. *11*, 3531. https://doi.org/10.1038/s41467-020-17324-z.

39. Toledo, L.I., Altmeyer, M., Rask, M.B., Lukas, C., Larsen, D.H., Povlsen, L.K., Bekker-Jensen, S., Mailand, N., Bartek, J., and Lukas, J. (2013). ATR prohibits replication catastrophe by preventing global exhaustion of RPA. Cell *155*, 1088–1103. https://doi.org/10.1016/j.cell.2013.10.043.

40. Jiang, G., Plo, I., Wang, T., Rahman, M., Cho, J.H., Yang, E., Lopez, B.S., and Xia, F. (2013). BRCA1-Ku80 protein interaction enhances end-joining fidelity of chromosomal double-strand breaks in the G1 phase of the cell cycle. J. Biol. Chem. *288*, 8966–8976. https://doi.org/10.1074/jbc.M112.412650.

41. Solier, S., Ryan, M.C., Martin, S.E., Varma, S., Kohn, K.W., Liu, H., Zeeberg, B.R., and Pommier, Y. (2013). Transcription poisoning by Topoisomerase I is controlled by gene length, splice sites, and miR-142-3p. Cancer Res. *73*, 4830–4839. https://doi.org/10.1158/0008-5472.CAN-12-3504.

42. Veloso, A., Biewen, B., Paulsen, M.T., Berg, N., Carmo de Andrade Lima, L., Prasad, J., Bedi, K., Magnuson, B., Wilson, T.E., and Ljungman, M. (2013). Genome-wide transcriptional effects of the anti-cancer agent camptothecin. PLoS One *8*, e78190. https://doi.org/10.1371/journal.pone.0078190.

43. Cristini, A., Groh, M., Kristiansen, M.S., and Gromak, N. (2018). RNA/DNA Hybrid Interactome Identifies DXH9 as a Molecular Player in Transcriptional Termination and R-Loop-Associated DNA Damage. Cell Rep. *23*, 1891–1905. https://doi.org/10.1016/j.celrep.2018.04.025.

44. Marinello, J., Arleo, A., Russo, M., Delcuratolo, M., Ciccarelli, F., Pommier, Y., and Capranico, G. (2022). Topoisomerase I poison-triggered immune gene activation is markedly reduced in human small-cell lung cancers by impairment of the cGAS/STING pathway. Br. J. Cancer *127*, 1214–1225. https://doi.org/10.1038/s41416-022-01894-4.

45. Powell, W.T., Coulson, R.L., Gonzales, M.L., Crary, F.K., Wong, S.S., Adams, S., Ach, R.A., Tsang, P., Yamada, N.A., Yasui, D.H., et al. (2013). R-loop formation at Snord116 mediates topotecan inhibition of Ube3a-antisense and allele-specific chromatin decondensation. Proc. Natl. Acad. Sci. USA *110*, 13938–13943. https://doi.org/10.1073/pnas.1305426110.

46. Groh, M., Lufino, M.M.P., Wade-Martins, R., and Gromak, N. (2014). R-loops associated with triplet repeat expansions promote gene

silencing in Friedreich ataxia and fragile X syndrome. PLoS Genet. *10*, e1004318. https://doi.org/10.1371/journal.pgen.1004318.

47. Boguslawski, S.J., Smith, D.E., Michalak, M.A., Mickelson, K.E., Yehle, C.O., Patterson, W.L., and Carrico, R.J. (1986). Characterization of monoclonal antibody to DNA.RNA and its application to immunodetection of hybrids. J. Immunol. Methods *89*, 123–130. https://doi.org/10.1016/0022-1759(86)90040-2.
48. Bou-Nader, C., Bothra, A., Garboczi, D.N., Leppla, S.H., and Zhang, J. (2022). Structural basis of R-loop recognition by the S9.6 monoclonal antibody. Nat. Commun. *13*, 1641. https://doi.org/10.1038/s41467-022-29187-7.
49. Sollier, J., Stork, C.T., García-Rubio, M.L., Paulsen, R.D., Aguilera, A., and Cimprich, K.A. (2014). Transcription-coupled nucleotide excision repair factors promote R-loop-induced genome instability. Mol. Cell *56*, 777–785. https://doi.org/10.1016/j.molcel.2014.10.020.
50. De Magis, A., Manzo, S.G., Russo, M., Marinello, J., Morigi, R., Sordet, O., and Capranico, G. (2019). DNA damage and genome instability by G-quadruplex ligands are mediated by R loops in human cancer cells. Proc. Natl. Acad. Sci. USA *116*, 816–825. https://doi.org/10.1073/pnas.1810409116.
51. Sanz, L.A., Hartono, S.R., Lim, Y.W., Steyaert, S., Rajpurkar, A., Ginno, P.A., Xu, X., and Chédin, F. (2016). Prevalent, Dynamic, and Conserved R-Loop Structures Associate with Specific Epigenomic Signatures in Mammals. Mol. Cell *63*, 167–178. https://doi.org/10.1016/j.molcel.2016.05.032.
52. Regairaz, M., Zhang, Y.W., Fu, H., Agama, K.K., Tata, N., Agrawal, S., Aladjem, M.I., and Pommier, Y. (2011). Mus81-mediated DNA cleavage resolves replication forks stalled by topoisomerase I-DNA complexes. J. Cell Biol. *195*, 739–749. https://doi.org/10.1083/jcb.201104003.
53. Strumberg, D., Pilon, A.A., Smith, M., Hickey, R., Malkas, L., and Pommier, Y. (2000). Conversion of topoisomerase I cleavage complexes on the leading strand of ribosomal DNA into 5'-phosphorylated DNA double-strand breaks by replication runoff. Mol. Cell Biol. *20*, 3977–3987. https://doi.org/10.1128/MCB.20.11.3977-3987.2000.
54. Harding, S.M., Benci, J.L., Irianto, J., Discher, D.E., Minn, A.J., and Greenberg, R.A. (2017). Mitotic progression following DNA damage enables pattern recognition within micronuclei. Nature *548*, 466–470. https://doi.org/10.1038/nature23470.
55. Lin, C.P., Ban, Y., Lyu, Y.L., and Liu, L.F. (2009). Proteasome-dependent processing of topoisomerase I-DNA adducts into DNA double strand breaks at arrested replication forks. J. Biol. Chem. *284*, 28084–28092. https://doi.org/10.1074/jbc.M109.030601.
56. Crossley, M.P., Song, C., Bocek, M.J., Choi, J.H., Kousouros, J.N., Sathirachinda, A., Lin, C., Brickner, J.R., Bai, G., Lans, H., et al. (2023). R-loop-derived cytoplasmic RNA-DNA hybrids activate an immune response. Nature *613*, 187–194. https://doi.org/10.1038/s41586-022-05545-9.
57. Mamouni, K., Cristini, A., Guirouilh-Barbat, J., Monferran, S., Lemarié, A., Faye, J.C., Lopez, B.S., Favre, G., and Sordet, O. (2014). RhoB promotes gammaH2AX dephosphorylation and DNA double-strand break repair. Mol. Cell Biol. *34*, 3144–3155. https://doi.org/10.1128/MCB.01525-13.
58. Menon, V., and Povirk, L.F. (2016). End-processing nucleases and phosphodiesterases: An elite supporting cast for the non-homologous end joining pathway of DNA double-strand break repair. DNA Repair *43*, 57–68. https://doi.org/10.1016/j.dnarep.2016.05.011.
59. Heo, J., Li, J., Summerlin, M., Hays, A., Katyal, S., McKinnon, P.J., Nitiss, K.C., Nitiss, J.L., and Hanakahi, L.A. (2015). TDP1 promotes assembly of non-homologous end joining protein complexes on DNA. DNA Repair *30*, 28–37. https://doi.org/10.1016/j.dnarep.2015.03.003.
60. Kawale, A.S., Akopiants, K., Valerie, K., Ruis, B., Hendrickson, E.A., Huang, S.Y.N., Pommier, Y., and Povirk, L.F. (2018). TDP1 suppresses mis-joining of radiomimetic DNA double-strand breaks and cooperates with Artemis to promote optimal nonhomologous end joining. Nucleic Acids Res. *46*, 8926–8939. https://doi.org/10.1093/nar/gky694.
61. Li, J., Summerlin, M., Nitiss, K.C., Nitiss, J.L., and Hanakahi, L.A. (2017). TDP1 is required for efficient non-homologous end joining in human cells. DNA Repair *60*, 40–49. https://doi.org/10.1016/j.dnarep.2017.10.003.
62. Hendrickson, E.A. (1997). Cell-cycle regulation of mammalian DNA double-strand-break repair. Am. J. Hum. Genet. *61*, 795–800. https://doi.org/10.1086/514895.
63. Das, B.B., Huang, S.y.N., Murai, J., Rehman, I., Amé, J.C., Sengupta, S., Das, S.K., Majumdar, P., Zhang, H., Biard, D., et al. (2014). PARP1-TDP1 coupling for the repair of topoisomerase I-induced DNA damage. Nucleic Acids Res. *42*, 4435–4449. https://doi.org/10.1093/nar/gku088.
64. Tsuda, M., Kitamasu, K., Kumagai, C., Sugiyama, K., Nakano, T., and Ide, H. (2020). Tyrosyl-DNA phosphodiesterase 2 (TDP2) repairs topoisomerase 1 DNA-protein crosslinks and 3'-blocking lesions in the absence of tyrosyl-DNA phosphodiesterase 1 (TDP1). DNA Repair *91–92*, 102849. https://doi.org/10.1016/j.dnarep.2020.102849.
65. Zeng, Z., Sharma, A., Ju, L., Murai, J., Umans, L., Vermeire, L., Pommier, Y., Takeda, S., Huylebroeck, D., Caldecott, K.W., and El-Khamisy, S.F. (2012). TDP2 promotes repair of topoisomerase I-mediated DNA damage in the absence of TDP1. Nucleic Acids Res. *40*, 8371–8380. https://doi.org/10.1093/nar/gks622.
66. Rashid, I., Hammel, M., Sverzhinsky, A., Tsai, M.S., Pascal, J.M., Tainer, J.A., and Tomkinson, A.E. (2021). Direct interaction of DNA repair protein tyrosyl DNA phosphodiesterase 1 and the DNA ligase III catalytic domain is regulated by phosphorylation of its flexible N-terminus. J. Biol. Chem. *297*, 100921. https://doi.org/10.1016/j.jbc.2021.100921.
67. Brettrager, E.J., Cuya, S.M., Tibbs, Z.E., Zhang, J., Falany, C.N., Aller, S.G., and van Waardenburg, R.C.A.M. (2023). N-terminal domain of tyrosyl-DNA phosphodiesterase I regulates topoisomerase I-induced toxicity in cells. Sci. Rep. *13*, 1377. https://doi.org/10.1038/s41598-023-28564-6.
68. He, X., van Waardenburg, R.C.A.M., Babaoglu, K., Price, A.C., Nitiss, K.C., Nitiss, J.L., Bjornsti, M.A., and White, S.W. (2007). Mutation of a conserved active site residue converts tyrosyl-DNA phosphodiesterase I into a DNA topoisomerase I-dependent poison. J. Mol. Biol. *372*, 1070–1081. https://doi.org/10.1016/j.jmb.2007.07.055.
69. Pinter, P., and Alpar, A. (2022). The Role of Extracellular Matrix in Human Neurodegenerative Diseases. Int. J. Mol. Sci. *23*. https://doi.org/10.3390/ijms231911085.
70. Nguyen, B., Bix, G., and Yao, Y. (2021). Basal lamina changes in neurodegenerative disorders. Mol. Neurodegener. *16*, 81. https://doi.org/10.1186/s13024-021-00502-y.
71. King, I.F., Yandava, C.N., Mabb, A.M., Hsiao, J.S., Huang, H.S., Pearson, B.L., Calabrese, J.M., Starmer, J., Parker, J.S., Magnuson, T., et al. (2013). Topoisomerases facilitate transcription of long genes linked to autism. Nature *501*, 58–62. https://doi.org/10.1038/nature12504.
72. Ljungman, M., and Hanawalt, P.C. (1996). The anti-cancer drug camptothecin inhibits elongation but stimulates initiation of RNA polymerase II transcription. Carcinogenesis *17*, 31–35. https://doi.org/10.1093/carcin/17.1.31.
73. Tresini, M., Warmerdam, D.O., Kolovos, P., Snijder, L., Vrouwe, M.G., Demmers, J.A.A., van IJcken, W.F.J., Grosveld, F.G., Medema, R.H., Hoeijmakers, J.H.J., et al. (2015). The core spliceosome as target and effector of non-canonical ATM signalling. Nature *523*, 53–58. https://doi.org/10.1038/nature14512.
74. Drolet, M., Broccoli, S., Rallu, F., Hraiky, C., Fortin, C., Massé, E., and Baaklini, I. (2003). The problem of hypernegative supercoiling and R-loop formation in transcription. Front. Biosci. *8*, d210–d221. https://doi.org/10.2741/970.
75. Li, X., and Manley, J.L. (2005). Inactivation of the SR protein splicing factor ASF/SF2 results in genomic instability. Cell *122*, 365–378. https://doi.org/10.1016/j.cell.2005.06.008.
76. Tuduri, S., Crabbé, L., Conti, C., Tourrière, H., Holtgreve-Grez, H., Jauch, A., Pantesco, V., De Vos, J., Thomas, A., Theillet, C., et al. (2009).

Topoisomerase I suppresses genomic instability by preventing interference between replication and transcription. Nat. Cell Biol. *11*, 1315–1324. https://doi.org/10.1038/ncb1984.

77. Manzo, S.G., Hartono, S.R., Sanz, L.A., Marinello, J., De Biasi, S., Cossarizza, A., Capranico, G., and Chedin, F. (2018). DNA Topoisomerase I differentially modulates R-loops across the human genome. Genome Biol. *19*, 100. https://doi.org/10.1186/s13059-018-1478-1.
78. Promonet, A., Padioleau, I., Liu, Y., Sanz, L., Biernacka, A., Schmitz, A.L., Skrzypczak, M., Sarrazin, A., Mettling, C., Rowicka, M., et al. (2020). Topoisomerase 1 prevents replication stress at R-loop-enriched transcription termination sites. Nat. Commun. *11*, 3940. https://doi.org/10.1038/s41467-020-17858-2.
79. El Hage, A., French, S.L., Beyer, A.L., and Tollervey, D. (2010). Loss of Topoisomerase I leads to R-loop-mediated transcriptional blocks during ribosomal RNA synthesis. Genes Dev. *24*, 1546–1558. https://doi.org/10.1101/gad.573310.
80. Shen, W., Sun, H., De Hoyos, C.L., Bailey, J.K., Liang, X.H., and Crooke, S.T. (2017). Dynamic nucleoplasmic and nucleolar localization of mammalian RNase H1 in response to RNAP I transcriptional R-loops. Nucleic Acids Res. *45*, 10672–10692. https://doi.org/10.1093/nar/gkx710.
81. Agarwal, V., and Kelley, D.R. (2022). The genetic and biochemical determinants of mRNA degradation rates in mammals. Genome Biol. *23*, 245. https://doi.org/10.1186/s13059-022-02811-x.
82. Katyal, S., el-Khamisy, S.F., Russell, H.R., Li, Y., Ju, L., Caldecott, K.W., and McKinnon, P.J. (2007). TDP1 facilitates chromosomal single-strand break repair in neurons and is neuroprotective in vivo. EMBO J. *26*, 4720–4731. https://doi.org/10.1038/sj.emboj.7601869.
83. Hawkins, A.J., Subler, M.A., Akopiants, K., Wiley, J.L., Taylor, S.M., Rice, A.C., Windle, J.J., Valerie, K., and Povirk, L.F. (2009). In vitro complementation of Tdp1 deficiency indicates a stabilized enzyme-DNA adduct from tyrosyl but not glycolate lesions as a consequence of the SCAN1 mutation. DNA Repair *8*, 654–663. https://doi.org/10.1016/j.dnarep.2008.12.012.
84. Guo, D., Dexheimer, T.S., Pommier, Y., and Nash, H.A. (2014). Neuroprotection and repair of 3'-blocking DNA ends by glaikit (gkt) encoding Drosophila tyrosyl-DNA phosphodiesterase 1 (TDP1). Proc. Natl. Acad. Sci. USA *111*, 15816–15820. https://doi.org/10.1073/pnas.1415011111.
85. Dunlop, J., Morin, X., Corominas, M., Serras, F., and Tear, G. (2004). glaikit is essential for the formation of epithelial polarity and neuronal development. Curr. Biol. *14*, 2039–2045. https://doi.org/10.1016/j.cub.2004.10.048.
86. Zaksauskaite, R., Thomas, R.C., van Eeden, F., and El-Khamisy, S.F. (2021). Tdp1 protects from topoisomerase 1-mediated chromosomal breaks in adult zebrafish but is dispensable during larval development. Sci. Adv. *7*, eabc4165. https://doi.org/10.1126/sciadv.abc4165.
87. Cristini, A., Tellier, M., Constantinescu, F., Accalai, C., Albulescu, L.O., Heiringhoff, R., Bery, N., Sordet, O., Murphy, S., and Gromak, N. (2022). RNase H2, mutated in Aicardi-Goutieres syndrome, resolves co-transcriptional R-loops to prevent DNA breaks and inflammation. Nat. Commun. *13*, 2961. https://doi.org/10.1038/s41467-022-30604-0.
88. McNeil, E.M., and Melton, D.W. (2012). DNA repair endonuclease ERCC1-XPF as a novel therapeutic target to overcome chemoresistance in cancer therapy. Nucleic Acids Res. *40*, 9990–10004. https://doi.org/10.1093/nar/gks818.
89. Kawale, A.S., and Povirk, L.F. (2018). Tyrosyl-DNA phosphodiesterases: rescuing the genome from the risks of relaxation. Nucleic Acids Res. *46*, 520–537. https://doi.org/10.1093/nar/gkx1219.
90. Cortes Ledesma, F., El Khamisy, S.F., Zuma, M.C., Osborn, K., and Caldecott, K.W. (2009). A human 5'-tyrosyl DNA phosphodiesterase that repairs topoisomerase-mediated DNA damage. Nature *461*, 674–678. https://doi.org/10.1038/nature08444.
91. Martins, S.G., Zilhão, R., Thorsteinsdóttir, S., and Carlos, A.R. (2021). Linking Oxidative Stress and DNA Damage to Changes in the Expression of Extracellular Matrix Components. Front. Genet. *12*, 673002. https://doi.org/10.3389/fgene.2021.673002.
92. Hoch, N.C., Hanzlikova, H., Rulten, S.L., Tétreault, M., Komulainen, E., Ju, L., Hornyak, P., Zeng, Z., Gittens, W., Rey, S.A., et al. (2017). XRCC1 mutation is associated with PARP1 hyperactivation and cerebellar ataxia. Nature *541*, 87–91. https://doi.org/10.1038/nature20790.
93. Dumitrache, L.C., and McKinnon, P.J. (2017). Polynucleotide kinase-phosphatase (PNKP) mutations and neurologic disease. Mech. Ageing Dev. *161*, 121–129. https://doi.org/10.1016/j.mad.2016.04.009.
94. Walker, C., Herranz-Martin, S., Karyka, E., Liao, C., Lewis, K., Elsayed, W., Lukashchuk, V., Chiang, S.C., Ray, S., Mulcahy, P.J., et al. (2017). C9orf72 expansion disrupts ATM-mediated chromosomal break repair. Nat. Neurosci. *20*, 1225–1235. https://doi.org/10.1038/nn.4604.
95. Skourti-Stathaki, K., Proudfoot, N.J., and Gromak, N. (2011). Human senataxin resolves RNA/DNA hybrids formed at transcriptional pause sites to promote Xrn2-dependent termination. Mol. Cell *42*, 794–805. https://doi.org/10.1016/j.molcel.2011.04.026.
96. Zhao, D.Y., Gish, G., Braunschweig, U., Li, Y., Ni, Z., Schmitges, F.W., Zhong, G., Liu, K., Li, W., Moffat, J., et al. (2016). SMN and symmetric arginine dimethylation of RNA polymerase II C-terminal domain control termination. Nature *529*, 48–53. https://doi.org/10.1038/nature16469.
97. Loomis, E.W., Sanz, L.A., Chédin, F., and Hagerman, P.J. (2014). Transcription-associated R-loop formation across the human FMR1 CGG-repeat region. PLoS Genet. *10*, e1004294. https://doi.org/10.1371/journal.pgen.1004294.
98. Daroui, P., Desai, S.D., Li, T.K., Liu, A.A., and Liu, L.F. (2004). Hydrogen peroxide induces topoisomerase I-mediated DNA damage and cell death. J. Biol. Chem. *279*, 14587–14594. https://doi.org/10.1074/jbc.M311370200.
99. Zhou, T., Lee, J.W., Tatavarthi, H., Lupski, J.R., Valerie, K., and Povirk, L.F. (2005). Deficiency in 3'-phosphoglycolate processing in human cells with a hereditary mutation in tyrosyl-DNA phosphodiesterase (TDP1). Nucleic Acids Res. *33*, 289–297. https://doi.org/10.1093/nar/gki170.
100. Nilsen, L., Forstrøm, R.J., Bjørås, M., and Alseth, I. (2012). AP endonuclease independent repair of abasic sites in Schizosaccharomyces pombe. Nucleic Acids Res. *40*, 2000–2009. https://doi.org/10.1093/nar/gkr933.
101. Barnham, K.J., Masters, C.L., and Bush, A.I. (2004). Neurodegenerative diseases and oxidative stress. Nat. Rev. Drug Discov. *3*, 205–214. https://doi.org/10.1038/nrd1330.
102. Smolka, J.A., Sanz, L.A., Hartono, S.R., and Chédin, F. (2021). Recognition of RNA by the S9.6 antibody creates pervasive artifacts when imaging RNA:DNA hybrids. J. Cell Biol. *220*, e202004079. https://doi.org/10.1083/jcb.202004079.
103. Alagia, A., Ketley, R.F., and Gullerova, M. (2022). Proximity Ligation Assay for Detection of R-Loop Complexes upon DNA Damage. Methods Mol. Biol. *2528*, 289–303. https://doi.org/10.1007/978-1-0716-2477-7_19.
104. Jeanblanc, M., Ragu, S., Gey, C., Contrepois, K., Courbeyrette, R., Thuret, J.Y., and Mann, C. (2012). Parallel pathways in RAF-induced senescence and conditions for its reversion. Oncogene *31*, 3072–3085. https://doi.org/10.1038/onc.2011.481.
105. Labrousse, G., Vande Perre, P., Parra, G., Jaffrelot, M., Leroy, L., Chibon, F., Escudie, F., Selves, J., Hoffmann, J.S., Guimbaud, R., and Lutzmann, M. (2023). The hereditary N363K POLE exonuclease mutant extends PPAP tumor spectrum to glioblastomas by causing DNA damage and aneuploidy in addition to increased mismatch mutagenicity. NAR Cancer *5*, zcad011. https://doi.org/10.1093/narcan/zcad011.
106. Al Abo, M., Sasanuma, H., Liu, X., Rajapakse, V.N., Huang, S.Y., Kiselev, E., Takeda, S., Plunkett, W., and Pommier, Y. (2017). TDP1 is Critical for the Repair of DNA Breaks Induced by Sapacitabine, a Nucleoside also Targeting ATM- and BRCA-Deficient Tumors. Mol. Cancer Therapeut. *16*, 2543–2551. https://doi.org/10.1158/1535-7163.MCT-17-0110.

107. Meisenberg, C., Gilbert, D.C., Chalmers, A., Haley, V., Gollins, S., Ward, S.E., and El-Khamisy, S.F. (2015). Clinical and cellular roles for TDP1 and TOP1 in modulating colorectal cancer response to irinotecan. Mol. Cancer Therapeut. *14*, 575–585. https://doi.org/10.1158/1535-7163.MCT-14-0762.

108. Munden, A., Benton, M.L., Capra, J.A., and Nordman, J.T. (2022). R-loop Mapping and Characterization During Drosophila Embryogenesis Reveals Developmental Plasticity in R-loop Signatures. J. Mol. Biol. *434*, 167645. https://doi.org/10.1016/j.jmb.2022.167645.

109. Agudelo, D., Duringer, A., Bozoyan, L., Huard, C.C., Carter, S., Loehr, J., Synodinou, D., Drouin, M., Salsman, J., Dellaire, G., et al. (2017). Marker-free coselection for CRISPR-driven genome editing in human cells. Nat. Methods *14*, 615–620. https://doi.org/10.1038/nmeth.4265.

110. Koczor, C.A., Saville, K.M., Andrews, J.F., Clark, J., Fang, Q., Li, J., Al-Rahahleh, R.Q., Ibrahim, M., McClellan, S., Makarov, M.V., et al. (2021). Temporal dynamics of base excision/single-strand break repair protein complex assembly/disassembly are modulated by the PARP/NAD(+)/SIRT6 axis. Cell Rep. *37*, 109917. https://doi.org/10.1016/j.celrep.2021.109917.

111. Kim, E., Ilic, N., Shrestha, Y., Zou, L., Kamburov, A., Zhu, C., Yang, X., Lubonja, R., Tran, N., Nguyen, C., et al. (2016). Systematic Functional Interrogation of Rare Cancer Variants Identifies Oncogenic Alleles. Cancer Discov. *6*, 714–726. https://doi.org/10.1158/2159-8290.CD-16-0160.

112. Weber, A.R., Krawczyk, C., Robertson, A.B., Kuśnierczyk, A., Vågbø, C.B., Schuermann, D., Klungland, A., and Schär, P. (2016). Biochemical reconstitution of TET1-TDG-BER-dependent active DNA demethylation reveals a highly coordinated mechanism. Nat. Commun. *7*, 10806. https://doi.org/10.1038/ncomms10806.

113. Barger, C.J., Branick, C., Chee, L., and Karpf, A.R. (2019). Pan-Cancer Analyses Reveal Genomic Features of FOXM1 Overexpression in Cancer. Cancers *11*, 251. https://doi.org/10.3390/cancers11020251.

114. Brinkman, E.K., Chen, T., Amendola, M., and van Steensel, B. (2014). Easy quantitative assessment of genome editing by sequence trace decomposition. Nucleic Acids Res. *42*, e168. https://doi.org/10.1093/nar/gku936.

115. Bery, N., Cruz-Migoni, A., Bataille, C.J., Quevedo, C.E., Tulmin, H., Miller, A., Russell, A., Phillips, S.E., Carr, S.B., and Rabbitts, T.H. (2018). BRET-based RAS biosensors that show a novel small molecule is an inhibitor of RAS-effector protein-protein interactions. Elife *7*, e37122. https://doi.org/10.7554/eLife.37122.

116. Bery, N., Legg, S., Debreczeni, J., Breed, J., Embrey, K., Stubbs, C., Kolasinska-Zwierz, P., Barrett, N., Marwood, R., Watson, J., et al. (2019). KRAS-specific inhibition using a DARPin binding to a site in the allosteric lobe. Nat. Commun. *10*, 2607. https://doi.org/10.1038/s41467-019-10419-2.

117. Gotzke, H., Kilisch, M., Martinez-Carranza, M., Sograte-Idrissi, S., Rajavel, A., Schlichthaerle, T., Engels, N., Jungmann, R., Stenmark, P., Opazo, F., and Frey, S. (2019). The ALFA-tag is a highly versatile tool for nanobody-based bioscience applications. Nat. Commun. *10*, 4403. https://doi.org/10.1038/s41467-019-12301-7.

118. Bery, N., Miller, A., and Rabbitts, T. (2020). A potent KRAS macromolecule degrader specifically targeting tumours with mutant KRAS. Nat. Commun. *11*, 3233. https://doi.org/10.1038/s41467-020-17022-w.

119. Patel, A.G., Flatten, K.S., Peterson, K.L., Beito, T.G., Schneider, P.A., Perkins, A.L., Harki, D.A., and Kaufmann, S.H. (2016). Immunodetection of human topoisomerase I-DNA covalent complexes. Nucleic Acids Res. *44*, 2816–2826. https://doi.org/10.1093/nar/gkw109.

120. Palminha, N.M., Dos Santos Souza, C., Griffin, J., Liao, C., Ferraiuolo, L., and El-Khamisy, S.F. (2022). Defective repair of topoisomerase I induced chromosomal damage in Huntington's disease. Cell. Mol. Life Sci. *79*, 160. https://doi.org/10.1007/s00018-022-04204-6.

121. Martin, M. (2011). Cutadapt removes adapter sequences from high-throughput sequencing reads. EMBnet. j. *17*, 10–12. https://doi.org/10.14806/ej.17.1.200.

122. Kim, D., Paggi, J.M., Park, C., Bennett, C., and Salzberg, S.L. (2019). Graph-based genome alignment and genotyping with HISAT2 and HISAT-genotype. Nat. Biotechnol. *37*, 907–915. https://doi.org/10.1038/s41587-019-0201-4.

123. Pertea, M., Pertea, G.M., Antonescu, C.M., Chang, T.C., Mendell, J.T., and Salzberg, S.L. (2015). StringTie enables improved reconstruction of a transcriptome from RNA-seq reads. Nat. Biotechnol. *33*, 290–295. https://doi.org/10.1038/nbt.3122.

124. Frankish, A., Diekhans, M., Ferreira, A.M., Johnson, R., Jungreis, I., Loveland, J., Mudge, J.M., Sisu, C., Wright, J., Armstrong, J., et al. (2019). GENCODE reference annotation for the human and mouse genomes. Nucleic Acids Res. *47*, D766–D773. https://doi.org/10.1093/nar/gky955.

125. Soneson, C., Love, M.I., and Robinson, M.D. (2015). Differential analyses for RNA-seq: transcript-level estimates improve gene-level inferences. F1000Res. *4*, 1521. https://doi.org/10.12688/f1000research.7563.2.

126. Ritchie, M.E., Phipson, B., Wu, D., Hu, Y., Law, C.W., Shi, W., and Smyth, G.K. (2015). limma powers differential expression analyses for RNA-sequencing and microarray studies. Nucleic Acids Res. *43*, e47. https://doi.org/10.1093/nar/gkv007.

127. Love, M.I., Huber, W., and Anders, S. (2014). Moderated estimation of fold change and dispersion for RNA-seq data with DESeq2. Genome Biol. *15*, 550. https://doi.org/10.1186/s13059-014-0550-8.

128. Wu, T., Hu, E., Xu, S., Chen, M., Guo, P., Dai, Z., Feng, T., Zhou, L., Tang, W., Zhan, L., et al. (2021). clusterProfiler 4.0: A universal enrichment tool for interpreting omics data. Innovation *2*, 100141. https://doi.org/10.1016/j.xinn.2021.100141.

129. Subramanian, A., Tamayo, P., Mootha, V.K., Mukherjee, S., Ebert, B.L., Gillette, M.A., Paulovich, A., Pomeroy, S.L., Golub, T.R., Lander, E.S., and Mesirov, J.P. (2005). Gene set enrichment analysis: a knowledge-based approach for interpreting genome-wide expression profiles. Proc. Natl. Acad. Sci. USA *102*, 15545–15550. https://doi.org/10.1073/pnas.0506580102.

130. McCann, J.L., Cristini, A., Law, E.K., Lee, S.Y., Tellier, M., Carpenter, M.A., Beghè, C., Kim, J.J., Sanchez, A., Jarvis, M.C., et al. (2023). APOBEC3B regulates R-loops and promotes transcription-associated mutagenesis in cancer. Nat. Genet. *55*, 1721–1734. https://doi.org/10.1038/s41588-023-01504-w.

131. Li, H. (2013). Aligning sequence reads, clone sequences and assembly contigs with BWA-MEM. Preprint at arXiv *888*. https://doi.org/10.48550/arXiv.1303.3997.

132. Danecek, P., Bonfield, J.K., Liddle, J., Marshall, J., Ohan, V., Pollard, M.O., Whitwham, A., Keane, T., McCarthy, S.A., Davies, R.M., and Li, H. (2021). Twelve years of SAMtools and BCFtools. GigaScience *10*, giab008. https://doi.org/10.1093/gigascience/giab008.

133. Ramirez, F., Ryan, D.P., Gruning, B., Bhardwaj, V., Kilpert, F., Richter, A.S., Heyne, S., Dundar, F., and Manke, T. (2016). deepTools2: a next generation web server for deep-sequencing data analysis. Nucleic Acids Res. *44*, W160–W165. https://doi.org/10.1093/nar/gkw257.

134. Miller, H.E., Montemayor, D., Abdul, J., Vines, A., Levy, S.A., Hartono, S.R., Sharma, K., Frost, B., Chédin, F., and Bishop, A.J.R. (2022). Quality-controlled R-loop meta-analysis reveals the characteristics of R-loop consensus regions. Nucleic Acids Res. *50*, 7260–7286. https://doi.org/10.1093/nar/gkac537.

135. Zhang, Y., Liu, T., Meyer, C.A., Eeckhoute, J., Johnson, D.S., Bernstein, B.E., Nusbaum, C., Myers, R.M., Brown, M., Li, W., and Liu, X.S. (2008). Model-based analysis of ChIP-Seq (MACS). Genome Biol. *9*, R137. https://doi.org/10.1186/gb-2008-9-9-r137.

136. Lee, S., Cook, D., and Lawrence, M. (2019). plyranges: a grammar of genomic data transformation. Genome Biol. *20*, 4. https://doi.org/10.1186/s13059-018-1597-8.

137. Morgan, M., and Shepherd, L. (2023). AnnotationHub: Client to Access AnnotationHub Resources. https://doi.org/10.18129/B9.bioc.AnnotationHub.

138. Pagès, H., Carlson, M., Falcon, S., and Li, N. (2023). AnnotationDbi: Manipulation of SQLite-Based Annotations in Bioconductor. https://doi.org/10.18129/B9.bioc.AnnotationDbi.

139. Stork, C.T., Bocek, M., Crossley, M.P., Sollier, J., Sanz, L.A., Chédin, F., Swigut, T., and Cimprich, K.A. (2016). Co-transcriptional R-loops are the main cause of estrogen-induced DNA damage. Elife *5*, e17548. https://doi.org/10.7554/eLife.17548.

140. Bery, N., and Rabbitts, T.H. (2019). Bioluminescence Resonance Energy Transfer 2 (BRET2)-Based RAS Biosensors to Characterize RAS Inhibitors. Curr. Protoc. Cell Biol. *83*, e83. https://doi.org/10.1002/cpcb.83.

STAR★METHODS

KEY RESOURCES TABLE

REAGENT or RESOURCE	SOURCE	IDENTIFIER
Antibodies		
p53BP1 (phospho-Ser1778) rabbit polyclonal antibody (used for: IF)	Cell Signaling Technology	Cat# 2675; RRID:AB_490917
Actin mouse monoclonal antibody (clone C4) (used for: WB)	Merck-Millipore	Cat# MAB1501; RRID:AB_2223041
ALFA sdAb HRP conjugated (used for: WB)	NanoTag Biotechnologies	Cat# N1501-HRP; N/A
ALFA Selector ST (nanobody ALFA-coupled agarose beads) (used for: IP)	NanoTag Biotechnologies	Cat# N1511; RRID:AB_3075991
CENPF (11) mouse monoclonal antibody (used for: IF)	Santa Cruz Biotechnology	Cat# sc-135865; RRID:AB_2076632
DNA ligase 3 (LIG3, DNL3) rabbit polyclonal antibody (used for: WB)	Bethyl	Cat# A301-636A; RRID:AB_1210932
DNA ligase 4 (LIG4) (D5N5N) rabbit monoclonal antibody (used for: WB)	Cell Signaling Technology	Cat# 14649; RRID:AB_2750871
dsDNA (double-stranded DNA) mouse monoclonal antibody (clone HYB331-01) (used for: Slot-blot)	Abcam	Cat# ab27156; RRID:AB_470907
FLAG DYKDDDDK Tag mouse monoclonal antibody (FG4R) (used for: WB in coIP exp)	Invitrogen	Cat# MA1-91878; RRID:AB_1957945
FLAG M2 mouse monoclonal antibody (used for: WB in Figures S7E and S7F)	Sigma-Aldrich	Cat# F1804; RRID:AB_262044
GFP goat antibody (used for: WB in Figures S7E and S7F)	Novus Biologicals	Cat# NB100-1770; RRID:AB_10128178
GFP rabbit polyclonal antibody (used for: WB in coIP exp)	Abcam	Cat# ab290; RRID: AB_303395
γH2AX (phospho-Ser139) mouse monoclonal antibody (clone JBW301) (used for: IF)	Merck-Millipore	Cat# 05–636; RRID:AB_309864
γH2AX (phospho-Ser139) rabbit monoclonal antibody (20E3) (used for: IF)	Cell Signaling Technology	Cat# 9718S; RRID:AB_2118009
HA-Tag (6E2) mouse monoclonal antibody HRP conjugated (used for: WB in coIP exp)	Cell Signaling Technology	Cat# 2999; RRID:AB_1264166
c-Myc (9E10) mouse monoclonal antibody (used for: WB in coIP exp)	Invitrogen	Cat# 13–2500; RRID:AB_2533008
c-Myc mouse monoclonal antibody (used for: WB in Figures S7E and S7F)	Takara Bio	Cat# 631206; RRID:AB_2928131
Nucleolin rabbit polyclonal antibody (used for: IF)	Abcam	Cat# ab22758; RRID:AB_776878
PARP1 rabbit polyclonal antibody (used for: WB)	Cell Signaling Technology	Cat# 9542; RRID:AB_2160739
PNKP (PNK1) rabbit polyclonal antibody (used for: WB)	Bethyl	Cat# A300-257A; RRID:AB_263356
S9.6 mouse monoclonal antibody (used for: DRIP, Slot-blot, PLA)	Merck-Millipore	Cat# MABE1095; RRID:AB_2861387
S9.6 mouse monoclonal antibody (used for: IF)	Giovanni Capranico laboratory	N/A; RRID:AB_2861387
TDP1 rabbit polyclonal antibody (used for: WB)	Abcam	Cat# ab224822; N/A
TDP2 rabbit polyclonal antibody (used for: WB)	Bethyl	Cat# A302-737A; RRID:AB_10631698
Topoisomerase I (TOP1) rabbit monoclonal antibody (EPR5375) (used for: WB, PLA)	Abcam	Cat# ab109374; RRID:AB_10861978

(*Continued on next page*)

Continued

REAGENT or RESOURCE	SOURCE	IDENTIFIER
Topoisomerase I-DNA Covalent Complexes (TOP1cc) mouse monoclonal antibody (used for: IF)	Merck-Millipore	Cat# MABE1084; RRID:AB_2756354
αTubulin mouse monoclonal antibody (used for: WB)	Sigma-Aldrich	Cat# T5168; RRID:AB_477579
XPF (ERCC4) rabbit polyclonal antibody (used for: WB)	Bethyl	Cat# A301-315A; RRID:AB_938089
XRCC1 rabbit polyclonal antibody (used for: WB)	Bethyl	Cat# A300-065A; RRID:AB_2218477
XRCC4 (RPL5) rabbit polyclonal antibody (used for: WB)	ABclonal	Cat# A1977; RRID:AB_2764003
Donkey anti-mouse secondary antibody, Alexa Fluor 488 (used for: IF)	ThermoFisher Scientific	Cat# A-21202; RRID:AB_141607
Goat anti-mouse secondary antibody, Alexa Fluor 488 (used for: IF S9.6)	ThermoFisher Scientific	Cat# A-11001; RRID:AB_2534069
Goat anti-rabbit secondary antibody, Alexa Fluor 594 (used for: IF)	ThermoFisher Scientific	Cat# A-11037; RRID:AB_2534095
Goat anti-mouse secondary antibody, Alexa Fluor 594 (used for: IF)	ThermoFisher Scientific	Cat# A-11032; RRID:AB_2534091
Goat anti-rabbit secondary antibody, Alexa Fluor 488 (used for: IF)	ThermoFisher Scientific	Cat# A-11070; RRID:AB_2534114
Goat anti-rabbit secondary antibody, Alexa Fluor 647 (used for: IF)	ThermoFisher Scientific	Cat# A-21245; RRID:AB_2535813
Goat anti-mouse secondary antibody, IgG (H + L)-HRP Conjugate (used for: WB)	Bio-Rad	Cat# 170-6516; RRID:AB_11125547
Goat anti-rabbit secondary antibody, IgG (H + L)-HRP Conjugate (used for: WB)	Bio-Rad	Cat# 1706515; RRID:AB_11125142
Horse anti-mouse IgG secondary antibody, HRP-linked (used for: WB)	Cell Signaling Technology	Cat# 7076; RRID:AB_330924
Chicken anti-goat IgG secondary antibody, HRP-linked (used for: WB)	ImmunoReagents	Cat# CkxGt-003-EHRPX; N/A
Chemicals, peptides, and recombinant proteins		
Benzonase	Sigma-Aldrich	Cat# E1014; CAS: 9025-65-4
BsaAI restriction enzyme	NEB	Cat# R0531S; N/A
Coelenterazine 400a	Cayman Chemicals	Cat# 16157; CAS: 70217-82-2
Complete mini EDTA-free protease inhibitor	Sigma-Aldrich	Cat# 11836170001; N/A
CPT [(S)-(+)-Camptothecin]	Sigma-Aldrich	Cat# C9911; CAS: 7689-03-4
CRISPR/Cas9 ribonucleoprotein complexes Alt-R S.p. Cas9 Nuclease V3	IDT	Cat# 1081058; N/A
Dharmafect 4 transfection reagent	Dharmacon/Horizon Discovery	Cat# T-2004; N/A
DRB	Sigma-Aldrich	Cat# D1916; CAS: 53-85-0
Doxycycline hyclate	Sigma-Aldrich	Cat# D9891; CAS 24390-14-5
Halt Protease & Phosphatase Inhibitor Cocktail	ThermoFisher Scientific	Cat# 1861281; N/A
JetPEI	Polyplus Transfection	Cat# 101000053
JetPRIME	Polyplus Transfection	Cat# 101000046
Lipofectamine™ RNAiMAX transfection reagent	ThermoFisher Scientific	Cat# 13778075
MG132 (Z-Leu-Leu-Leu-al)	Sigma-Aldrich	Cat# C221; CAS: 133407-82-6
NU7441 (KU57788)	Tocris	Cat# 3712; CAS: 503468-95-9
Ouabain octahydrate	Sigma-Aldrich	Cat# O3125; CAS: 11018-89-6
Phosphatase inhibitor PhosStop	Roche	Cat# 04906845001; N/A
Phusion High-Fidelity DNA Polymerase	ThermoFisher Scientific	Cat# M0530; N/A
Polybrene	Sigma-Aldrich	Cat# 107689; CAS: 28728-55-4

(*Continued on next page*)

Continued

REAGENT or RESOURCE	SOURCE	IDENTIFIER
Poly-L-lysine solution	Sigma-Aldrich	Cat# P4832; CAS: 25988-63-0
Protein A dynabeads	Invitrogen	Cat# 10002D
Proteinase K	Sigma-Aldrich	Cat# 3115828001; N/A
Puromycin	InvivoGen	Cat# ant-pr-1; CAS: 58-58-2
RNase H	NEB	Cat# M0297; N/A
Selector Control (for: coIP exp)	NanoTag Biotechnologies	Cat# N0010
Critical commercial assays		
Click-iT RNA Alexa Fluor 488 Imaging Kit	ThermoFisher Scientific	Cat# C10329
Click-iT EdU Alexa Fluor 647 Imaging Kit	ThermoFisher Scientific	Cat# C10340
Duolink PLA probe anti-mouse minus	Sigma-Aldrich	Cat# DUO92004
Duolink PLA probe anti-rabbit plus	Sigma-Aldrich	Cat# DUO92002
Duolink *In Situ* Detection Reagents Green	Sigma-Aldrich	Cat# DUO92014
Duolink *In Situ* Mounting Medium with DAPI	Sigma-Aldrich	Cat# DUO82040
GenElute Mammalian Genomic DNA miniprep kit	Sigma-Aldrich	Cat# G1N70-1KT
iScript cDNA synthesis kit	Bio-Rad	Cat# 1708891
IQ SYBR green Supermix	Bio-Rad	Cat# 1708880
MinElute^{TM} PCR purification Kit	QIAGEN	Cat# 28004
NEBNext Ultra Directional RNA Library Prep Kit for Illumina	NEB	Cat# E7420S
QIAquick PCR purification kit	QIAGEN	Cat# 28104
RNeasy Plus Mini Kit	QIAGEN	Cat# 74134
Ribo-Zero rRNA Removal Kit	Illumina	Cat# 20040529
Deposited data		
DRIP-seq datasets	This paper	GEO: GSE226263
RNA-seq datasets	This paper	GEO: GSE186693
Experimental models: Cell lines		
Human: HEK293T cells	ATCC	Cat# CRL-3216; RRID:CVCL_0063
Human: U2OS cells	ATCC	Cat# HTB-96; RRID:CVCL_0042
Human: U2OS TDP1^{H493R} cells (SCAN1$^{\#1}$, SCAN1$^{\#2}$)	This paper; Olivier Sordet laboratory	N/A
Human: U2OS TDP1 KO cells	This paper; Olivier Sordet laboratory	N/A
Human: U2OS cells inducible for 3xFLAG-TDP1	This paper; Olivier Sordet laboratory	N/A
Human: U2OS TDP1^{H493R} cells (SCAN1$^{\#1}$, SCAN1$^{\#2}$) inducible for 3xFLAG-TDP1	This paper; Olivier Sordet laboratory	N/A
Human: WI38-hTERT cells	Carl Mann laboratory; Jeanblanc et al.[104]	N/A
Drosophila melanogaster: Schneider 2 (S2) cells	Luisa di Stefano laboratory	N/A
Oligonucleotides		
DNA ligase 3 (LIG3, DNL3) (human) SMARTpool siRNA	Dharmacon/Horizon Discovery	Cat# M-009227-02
DNA ligase 4 (LIG4) (human) SMARTpool siRNA	Dharmacon/Horizon Discovery	Cat# M-004254-00
PARP1 (human) SMARTpool siRNA	Dharmacon/Horizon Discovery	Cat# M-006656-01
PNKP (human) SMARTpool siRNA	Dharmacon/Horizon Discovery	Cat# M-006783-02
TDP1 (human) SMARTpool siRNA	Dharmacon/Horizon Discovery	Cat# M-016112-01
TDP2 (human) SMARTpool siRNA	Dharmacon/Horizon Discovery	Cat# M-017578-00
XPF (human) (ERCC4) SMARTpool siRNA	Dharmacon/Horizon Discovery	Cat# M-019946-00
XRCC1 (human) SMARTpool siRNA	Dharmacon/Horizon Discovery	Cat# M-009394-01
XRCC4 (human) SMARTpool siRNA	Dharmacon/Horizon Discovery	Cat# M-004494-02
Firefly luciferase control sequence	Dharmacon/Horizon Discovery	Cat# D-001400-01

(*Continued on next page*)

Continued

REAGENT or RESOURCE	SOURCE	IDENTIFIER
gRNA for *ATP1A1*	IDT; Sequence is reported in Labrousse et al.[105]	N/A
gRNA *TDP1* exon 5: 5′- GTTTAACTACTGCTTTGACG -3′	IDT; Sequence is reported in Abo et al.[106]	N/A
gRNA *TDP1* exon 14: 5′-TATGTGGC ATGGCATTGCTG-3′	IDT; This paper	N/A
ssODNs donor for *ATP1A1*-RD	IDT; Sequence is reported in Labrousse et al.[105]	N/A
ssODNs donor for *TDP1* exon 14: 5′-CTTCCCTATAGCATCCAGAC AGCTGAAAAACAGAATTGGCTGCA TTCCTATTTTCACAAATGGTCAGCTG AGACGTCTGGTCGCAGCAATGCCA TGCCACGTATTAAGACATATATGAG GCCTTCTCCAGACTTCAGT-3′	IDT; This paper	N/A
ssODNs donor for *TDP1* exon 5: 5′- CTT CTTTTCTCCCATCTAGTTTAACTACTGC TTTGACGTAGACTGGCTCGTATAACAG TATCCACCAGAGTTCAGGTGACGTCCT CAGGGTGACAGACAACACTATAAACTGTAAA -3′	IDT; This paper	N/A
Primer qRT-PCR, *TDP1* e3-e5 (F):5′- CCCCTTCCAGTTTTACCTCAC -3′	Eurogentec; Sequence is reported in Meisenberg et al.[107]	N/A
Primer qRT-PCR, *TDP1* e3-e5 (R):5′- AGTCCACGTCAAAGCAGTAG -3′	Eurogentec; Sequence is reported in Meisenberg et al.[107]	N/A
Primer qRT-PCR, *GAPDH* (F):5′- ACATCAAGAAGGTGGTGAAG -3′	Eurogentec; Sequence is reported in Cristini et al.[87]	N/A
Primer qRT-PCR, *GAPDH* (R):5′- GGGTCTTACTCCTTGGAGGC -3′	Eurogentec; Sequence is reported in Cristini et al.[87]	N/A
Primer DRIP-qPCR, *ACT5C*-Drosophila (F):5′- CCACGAGACCACCTACAACT -3′	Eurogentec; Sequence is reported in Munden et al.[108]	N/A
Primer DRIP-qPCR, *ACT5C*-Drosophila (R):5′- TGATCTTCATGGTCGACGGT -3′	Eurogentec; Sequence is reported in[108]	N/A
See Table S2 for other primers used in this study.	Eurogentec; This paper	N/A
Recombinant DNA		
Plasmid: eSpCas9(1.1)_No_FLAG_ATP1A1_ G3_Dual_sgRNA	Agudelo et al.[109]	Addgene; #86613
Plasmid: eSpCas9(1.1)_No_FLAG_ATP1A1_ G3_Dual_sgRNA_TDP1_exon14	This paper	N/A
Plasmid: eSpCas9(1.1)_No_FLAG_ATP1A1_ G3_Dual_sgRNA_TDP1_exon5	This paper	N/A
Plasmid: ATP1A1-RD	Agudelo et al.[109]	Addgene; #86551
Plasmid: pLV-CMV-XRCC1-EGFP-Hygro	Koczor et al.[110]	Addgene; #176062
Plasmid: pDONR223_PNKP_WT	*Kim* et al.[111]	Addgene; #81801
Plasmid: pGEX4T-hLIG3	Weber et al.[112]	Addgene; #81055
Plasmid: TLCV2	Barger et al.[113]	Addgene; #87360
Plasmid: TLCV2-3xFLAG-TDP1	This paper	N/A
Plasmid: pEF-3xFLAG-TDP1	This paper	N/A
Plasmid: pEF-3xFLAG-TDP1^{H493R}	This paper	N/A
Plasmid: pEF-GFP^{2}-TDP1	This paper	N/A
Plasmid: pEF-GFP^{2}-TDP1^{H493R}	This paper	N/A
Plasmid: pEF-TDP2-GFP^{2}	This paper	N/A
Plasmid: pEF-XRCC1-ALFA	This paper	N/A

(*Continued on next page*)

Continued

REAGENT or RESOURCE	SOURCE	IDENTIFIER
Plasmid: pEF-HA-LIG3α	This paper	N/A
Plasmid: pEF-TDP2-myc	This paper	N/A
Plasmid: pEF-3xFLAG-PNKP	This paper	N/A
Plasmid: pEF-myc-cyto	Invitrogen	Cat# V89120
Plasmid: pEF-RLuc8-LIG3α	This paper	N/A
Software and algorithms		
A plasmid Editor (ApE) software	M.Wayne Davis	https://jorgensen.biology.utah.edu/wayned/ape/ RRID:SCR_014266
Bio-Rad CFX Manager 3.1	Bio-Rad	Cat# 1845000 https://www.bio-rad.com/fr-fr/sku/1845000-cfx-manager-software?ID=1845000 RRID:SCR_017251
Columbus software (version 2.8.2)	PerkinElmer	N/A
GraphPad Prism 10	GraphPad Prism	http://www.graphpad.com/; RRID:SCR_002798
Harmony software (version 4.9)	PerkinElmer	RRID:SCR_023543
ImageJ software (version 1.53.o)	National Institutes of Health	https://imagej.nih.gov/ij/; RRID:SCR_003070
ImageLab software (version 6.0.1)	National Institutes of Health	https://imagej.nih.gov/ij/; RRID:SCR_003070
TIDE	Brinkman et al.[114]	https://tide.nki.nl RRID:SCR_023704
Other		
AxioObserver Z1 fluorescence microscope	ZEISS	https://www.zeiss.com
4D-Nucleofector X Unit, FL1	Lonza	Cat# AAF-1002B
4D-Nucleofector Core Unit, FL1	Lonza	Cat# AAF-1002X
Bioruptor sonicator	Diagenode	Cat# B01020001
CellCarrier Ultra 96-well	PerkinElmer	Cat# 6005550
Phenoplate 96-well	PerkinElmer	Cat# 6055300
White 96-well plates, clear bottom	PerkinElmer	Cat# 6005181
ChemiDoc MP Imaging System	Bio-Rad	https://www.bio-rad.com
CLARIOstar microplate reader	BMG Labtech	https://www.bmglabtech.com
CFX96™ real-time system device	Bio-Rad	https://www.bio-rad.com
LSM 880 confocal microscope	ZEISS	https://www.zeiss.com
Eclipse 90i Microscope	Nikon	https://www.microscope.healthcare.nikon.com/
Operetta CLS High-Content Imaging System	PerkinElmer	https://www.perkinelmer.com
Tetracycline-free FBS	Takara Bio	Cat# 631106
Schneider's Drosophila Medium	Gibco	Cat# 21720024

RESOURCE AVAILABILITY

Lead contact

Further information and requests for resources and reagents should be directed to and will be fulfilled by the lead contact, Olivier Sordet (olivier.sordet@inserm.fr).

Materials availability

Engineered cell lines [U2OS TDP1^{H493R} cells (SCAN1$^{\#1}$, SCAN1$^{\#2}$), U2OS TDP1 KO cells, U2OS cells inducible for 3xFLAG-TDP1, U2OS TDP1^{H493R} cells (SCAN1$^{\#1}$, SCAN1$^{\#2}$) inducible for 3xFLAG-TDP1] and plasmids [eSpCas9(1.1)_No_FLAG_ATP1A1_G3_Dual_sgRNA_TDP1_exon14, eSpCas9(1.1)_No_FLAG_ATP1A1_G3_Dual_sgRNA_TDP1_exon5, pEF-3xFLAG-TDP1, pEF-3xFLAG-TDP1^{H493R}, pEF-GFP^2-TDP1, pEF-GFP^2-TDP1^{H493R}, pEF-TDP2-GFP^2, TLCV2-3xFLAG-TDP1, pEF-XRCC1-ALFA, pEF-HA-LIG3α,

pEF-TDP2-myc, pEF-3xFLAG-PNKP, pEF-RLuc8-LIG3α] generated in this study will be available without restrictions upon request: lead contact, Olivier Sordet (olivier.sordet@inserm.fr).

Data and code availability

- This paper generated RNA-seq datasets available at Gene Expression Omnibus GSE186693, and DRIP-seq datasets available at Gene Expression Omnibus GSE226263.
- This paper does not report original code.
- Any additional information required to reanalyze the data reported in this work paper is available from the lead contact upon request.

EXPERIMENTAL MODEL AND STUDY PARTICIPANT DETAILS

Cells and treatments

Human U2OS cells (from a 15-year-old female) and human HEK293T embryonic kidney cells (from a female fetus) were obtained from the American Type Culture Collection (ATCC), and grown in Dulbecco's Modified Eagle's Medium (DMEM) supplemented with 10% (v/v) fetal bovine serum and 1% (v/v) penicillin/streptomycin at 37°C in 5% CO_2. Primary human lung embryonic WI38 fibroblasts (from a 3-month-gestation aborted female fetus) immortalized with hTERT were obtained from Carl Mann (CEA, Gif-sur-Yvette, France).[104] Cells were grown in Modified Eagle's Medium (MEM) supplemented with 10% (v/v) fetal bovine serum, 1 mM sodium pyruvate, 2 mM glutamine and 0.1 mM non-essential amino acids at 37°C in 5% CO_2. To induce quiescence, cells were washed twice with serum-free medium and cultured for 72 h in medium supplemented as described above but with 0.2% (v/v) serum, as previously described.[31,32] *Drosophila* Schneider 2 (S2) cells were obtained from Luisa Di Stefano (Centre de Biologie Intégrative, Toulouse) and grown at 28°C in Schneider's Drosophila Medium (#21720024; Gibco) containing 10% (v/v) heat-inactivated fetal bovine serum. Drugs and chemicals used for treatments were ouabain (#O3125), CPT (#C9911), doxycycline (#D9891), DRB (#D1916) and MG132 (#C2211) from Sigma-Aldrich and NU7441 from Tocris (#3712). All these agents were dissolved in DMSO except ouabain and doxycycline, which were in water. In all the experiments, mock samples were treated with the vehicle only.

METHOD DETAILS

Generation of U2OS cells *TDP1* H493R (SCAN1) and *TDP1* KO

To generate U2OS cells carrying the TDP1 H493R mutation, we introduced the homozygous endogenous point mutation in exon 14 of *TDP1* gene (A1478G) found in SCAN1 patients[5] using CRISPR-Cas9 genome editing. To enrich for custom genetic modifications, the strategy used was the targeting of *TDP1* gene together with *ATP1A1* gene, which makes cells resistant to ouabain after recombination with a donor DNA (ATP1A1-RD) containing ouabain-resistant mutations.[109] The guide RNA (gRNA) targeting the protospacer of exon 14 on *TDP1* gene (5′-TATGTGGCATGGCATTGCTG-3′) was designed using CRISPOR (http://crispor.tefor.net) to produce a DSB by Cas9 close to the A1478 residue. Then, two different transfection strategies were used to generate the two SCAN1 clones.

To generate U2OS SCAN1$^{\#2}$, cells were co-transfected using jetPEI (#101000053; Polyplus Transfection) with i) a plasmid expressing both the eSpCas9 and a gRNA targeting the protospacer on the *ATP1A1* gene (eSpCas9(1.1)_No_FLAG_ATP1A1_G3_Dual_sgRNA plasmid; #86613; Addgene),[109] in which, the gRNA targeting *TDP1* exon 14 was inserted (eSpCas9(1.1)_No_FLAG_ATP1A1_G3_Dual_sgRNA_TDP1_exon14); ii) an ATP1A1-RD plasmid donor (#86551; Addgene),[109] and iii) a single-stranded oligodeoxyribonucleotides (ssODNs) donor for *TDP1* exon 14 (5′-CTTCCCTATAGCATCCAGACAGCTGAAAAACAGAATTGGCTGCATTCCTATTTTCACAAATGGTCAGCTGAGACGTCTGGTCGCAGCAATGCCATGCCACGTATTAAGACATATATGAGGCCTTCTCCAGACTTCAGT-3'; Ultramer DNA oligonucleotides; IDT) with homology arms for the *TDP1*-targeted site and containing the mutations to substitute A1478 by G1478[5] and to mutate the PAM sequence after DSB repair by homologous recombination.

To generate U2OS SCAN1$^{\#1}$, cells were electroporated with the Amaxa Nucleofector system (Lonza) to codeliver i) CRISPR-Cas9 ribonucleoprotein complexes (Alt-R S.p. Cas9 Nuclease V3; #1081058; IDT) together with a gRNA for *ATP1A1* gene (Alt-R CRISPR-Cas9 sgRNA; IDT) and a gRNA for *TDP1* exon 14 (Alt-R CRISPR-Cas9 sgRNA; IDT); ii) a ssODNs donor for *TDP1* exon 14 (Ultramer TM DNA oligonucleotides; IDT), and iii) ssODNs donor for *ATP1A1-RD* (Ultramer DNA oligonucleotides; IDT).[109] Cells were cultured, 4 h before and 24 h after electroporation, in medium supplemented with 2 μM of the DNA-PK inhibitor NU7441 (#3712; Tocris) to inhibit NHEJ repair.

To select cells in which genome editing has occurred, 0.7 μM ouabain (#O3125; Sigma-Aldrich) was added to the culture medium three days after transfection or electroporation. The obtained ouabain-resistant cell clones were then screened by extracting genomic DNA with GenElute Mammalian Genomic DNA miniprep kit (#G1N70-1KT; Sigma-Aldrich). The targeted regions were amplified by using the Phusion High-Fidelity DNA Polymerase (#M0530; ThermoFisher Scientific) with primers targeting *TDP1* exon 14 (Table S2). The A1478G mutation generated a new restriction site for BsaAI restriction enzyme, and therefore, homozygosity was assessed by digestion of the amplicons with BsaAI (#R0531S; NEB).

To generate U2OS *TDP1* KO cells, *TDP1* exon 5 was targeted using CRISPR-Cas9 genome editing, as previously described.[106] Cells were transfected using jetPEI (#101000053; Polyplus Transfection) with i) a plasmid expressing both the eSpCas9 and a gRNA targeting the protospacer on the *ATP1A1* gene (eSpCas9(1.1)_No_FLAG_ATP1A1_G3_Dual_sgRNA plasmid; #86613;

Addgene),[109] in which the gRNA targeting *TDP1* exon 5 (5′-GTTTAACTACTGCTTTGACG-3′)[106] was inserted (eSpCas9(1.1)_No_-FLAG_ATP1A1_G3_Dual_sgRNA_TDP1_exon5); ii) an ATP1A1-RD plasmid donor (#86551; Addgene),[109] and iii) a ssODNs donor for *TDP1* exon 5 (5′-CTTCTTTTCTCCCATCTAGTTTAACTACTGCTTTGACGTAGACTGGCTCGTATAACAGTATCCACCAGAGTT CAGGTGACGTCCTCAGGGTGACAGACAACACTATAAACTGTAAA-3′) with homology arms for the *TDP1*-targeted site and containing mutations to insert a stop codon and to mutate the PAM sequence after DSB repair by homologous recombination. Ouabain-resistant cell clones were obtained and screened as described for SCAN1 clones, by using primers targeting *TDP1* exon 5 (Table S2).

CRISPR editing was verified by chromatogram analysis using the ApE software (https://jorgensen.biology.utah.edu/wayned/ape/) and TIDE (https://tide.nki.nl) analysis.

Molecular cloning

XRCC1 (Addgene plasmid #176062),[110] PNKP (Addgene plasmid #81801),[111] LIG3α (Addgene plasmid #81055),[112] TDP1 and TDP2 (extracted directly from U2OS cells cDNA) were amplified by PCR and inserted into the appropriate plasmids. TDP1^{H493R} was generated by PCR site-directed mutagenesis using wild-type TDP1 as template.

BRET vector construction

TDP1 and TDP1^{H493R} were cloned between NotI/XbaI sites of the pEF-GFP^2-MCS,[115] and TDP2 was cloned between NcoI/XhoI sites in pEF-MCS-GFP^2,[115] to obtain pEF-GFP^2-$(GGGGS)_1$-TDP1/TDP1$^{(H493R)}$ and pEF-TDP2-$(GGGGS)_2$-GFP^2, respectively. LIG3α was inserted between NotI/XbaI sites of the pEF-RLuc8-MCS[115] to obtain pEF-RLuc8-$(GGGGS)_2$-LIG3α.

Tagged protein vector construction

TDP1, TDP1^{H493R} and PNKP were cloned into the pEF-3xFLAG-MCS[116] by PCR using NotI/XbaI sites. XRCC1 was cloned into pEF-myc-cyto plasmid (#V89120; Invitrogen) between PmlI/XhoI sites and ALFA tag[117] was added in fusion to XRCC1 by cloning between XhoI/XbaI sites to make pEF-XRCC1-ALFA. TDP2 was inserted into pEF-myc-cyto plasmid between NcoI/XhoI sites to generate pEF-TDP2-myc. LIG3α was cloned into pEF-myc-cyto between NotI/XbaI sites and HA tag was added in fusion to LIG3α by cloning between PmlI/NotI sites and generate pEF-HA-LIG3α.

Lentivector construction

3xFLAG-TDP1 sequence was inserted between AgeI/NheI sites of TLCV2 lentivector (Addgene plasmid #87360)[113] by PCR.

Generation of U2OS cells inducible for 3xFLAG-TDP1

Lentiviral particles production and transduction was adapted from.[118] Briefly, 4.5 x 10^6 HEK293T cells were plated in a 100 mm dish (2 dishes per virus production). 24 h later, cells were transfected with 6 μg of TLCV2-3xFLAG-TDP1, 4 μg of psPAX2 and 1.5 μg of pMD2.G and 23 μL of JetPRIME transfection reagent (#101000046; Polyplus Transfection) (quantities for one 100 mm dish). The supernatants were collected 48 h after transfection, centrifuged 5 min at 2,000 rpm, filtered (0.45 μm filter) and concentrated by centrifugation at 2,500 rpm using a 100 kDa cut-off Vivaspin 20 concentrator (Sartorius). U2OS cells (WT, SCAN1$^{\#1}$ and SCAN1$^{\#2}$) were transduced with 3xFLAG-TDP1 lentivirus for 48 h in 6-well plate in 1 mL of medium containing 8 μg/mL of polybrene (#107689; Sigma-Aldrich). Transduced cells were selected with 1 μg/mL puromycin (#ant-pr-1; InvivoGen). 0.1 μg/mL of doxycycline (#D9891; Sigma-Aldrich) was added to the culture medium supplemented with 10% (v/v) tetracycline-free FBS (#631106; Takara Bio) for 48 h to induce the expression of 3xFLAG-TDP1.

Cell extracts and immunoblotting

Cell extracts were obtained by lysing cells for 20 min at 4°C in buffer containing 50 mM Tris-HCl (pH 8.0), 150 mM NaCl, 1% Triton X-100, 1% sodium deoxycholate, 0.1% SDS, 5 mM EDTA, supplemented with protease and phosphatase inhibitors (Halt Protease & Phosphatase Inhibitor Cocktail; ThermoFisher Scientific). Samples were centrifuged at 16,000 x g for 15 min at 4°C and supernatant was collected. For Figures 1D, 6F, S4H, S6F and S7B, cell extracts were obtained by lysing cells for 15 min at 4°C in buffer containing 10 mM Tris-HCl (pH 7.5), 1% SDS supplemented with protease and phosphatase inhibitors (Halt Protease & Phosphatase Inhibitor Cocktail; ThermoFisher Scientific). Viscosity of the samples was reduced by sonication. Proteins were separated by SDS-PAGE and immunoblotted with the following antibodies at dilutions recommended by the manufacturer: anti-pan-actin (#MAB1501; Merck-Millipore), anti-DNA ligase 3 (#A301-636A; Bethyl), anti-DNA ligase 4 (#14649; Cell Signaling Technology), anti-FLAG (#F1804; Sigma-Aldrich), anti-PARP1 (#9542; Cell Signaling Technology), anti-PNKP (#A300-257A; Bethyl), anti-TDP1 (#ab224822; Abcam), anti-TDP2 (#A302-737A; Bethyl), anti-TOP1 (#ab109374; Abcam), anti-αTubulin (#T5168; Sigma-Aldrich), anti-XPF (#A301315A; Bethyl); anti-XRCC1 (#A300-065A; Bethyl), anti-XRCC4 (#A1977; Abclonal), anti-GFP (#NB100-1770; Novus Biologicals) and anti-c-Myc (#631206; Takara Bio). The membrane was then incubated with the appropriate secondary antibody coupled to HRP (Bio-Rad, Cell Signaling Technology, ImmunoReagents) for 1 h, and immunoblotting was revealed by chemiluminescence using a ChemiDoc MP Imaging System (Bio-Rad). Quantification of protein levels was done by using ImageLab software (version 6.0.1).

RNA analysis by qRT-PCR

Total RNA was isolated using RNeasy Plus Mini Kit (#74134; QIAGEN) according to the manufacturer's instructions. 0.5–1 μg of total RNA were reverse transcribed by using the iScript cDNA synthesis kit (#1708891; Bio-Rad) and analyzed by quantitative PCR on a CFX96 real-time system device (Bio-Rad) by using IQ SYBR green Supermix (#1708880; Bio-Rad) according to the manufacturer's

protocol. Values are normalized to *GAPDH* mRNA, used as an endogenous control in the $\Delta\Delta C_T$ analysis with the Bio-Rad CFX Manager 3.1. The primers used in this study are listed in Table S2.

Immunofluorescence microscopy of TOP1cc

TOP1cc staining was performed using a previously described method[119] with modifications.[120] Briefly, cells were seeded on coverslips in 6-well plates, washed twice with phosphate-buffered saline (PBS) and fixed with 10% formalin for 15 min at 4°C. After three washes with PBS, cells were permeabilized with 0.2% Triton X-100 for 2 min on ice, followed by an incubation in 0.1% SDS for 5 min at RT. Cells were then washed twice in PBS, incubated for 1 h in a blocking buffer containing 10% (w/v) skimmed milk, 150 mM NaCl and 10 mM Tris–HCl (pH 7.4), and incubated with a mouse anti-TOP1cc antibody (#MABE1084; Merck-Millipore) diluted at 1/1,000 in 5% (v/v) fetal bovine serum in PBS overnight at 4°C. Next, cells were washed five times for 4 min each with wash buffer (0.1% bovine serum albumin (BSA) and 0.1% Triton X-100 in PBS) and incubated with an anti-mouse antibody coupled to Alexa Fluor 488 (#A-21202; ThermoFisher Scientific) diluted at 1/1,000 in 5% (v/v) fetal bovine serum in PBS for 1 h at RT. After five washes for 4 min each with wash buffer, coverslips were mounted in glass slides using Mowiol 4–88 (Merck-Millipore) containing 4′,6-diamidino-2-phenylindole (DAPI) diluted at 1/2,000. Slides were visualized with an inverted confocal microscope (LSM 880; ZEISS) using a 63× oil immersion objective. Nuclear foci were analyzed with ImageJ software (version 1.53o).

For graphical representation of foci distribution, we used box-and-whisker plots with GraphPad Prism 10 software with the following settings: boxes: 25–75 percentile range; whiskers: 10–90 percentile range; horizontal bars: median number of foci; ''+'': mean number of foci.

Quantification of global nascent RNA transcription

Cells were seeded in poly-L-lysine (#P4832; Sigma-Aldrich)-coated 96-well plates (CellCarrier Ultra: #6005550; PerkinElmer). Global nascent RNA transcription was detected using Click-iT RNA Alexa Fluor 488 Imaging Kit (#C10329, ThermoFisher Scientific) following manufacturer's guidelines. After Click-iT reaction, cells were incubated with 8% (w/v) BSA in PBS for 1 h before incubation with an anti-nucleolin antibody (#ab22758; Abcam) diluted at 1/1,000 in 1% BSA in PBS for 1 h at RT. After three washes with PBS, cells were incubated with the secondary antibody coupled to Alexa Fluor 647 (#A-21245; ThermoFisher Scientific) diluted at 1/500 in 1% BSA in PBS for 1 h. After three washes with PBS, nuclei were stained with 1 mg/mL Hoechst 33342 (ThermoFisher Scientific) for 15 min, washed twice with PBS and stored at 4°C until analysis. Plates were scanned with a 20× objective using an Operetta CLS High-Content Imaging System (PerkinElmer) with Harmony software (version 4.9). Analyses were performed with Columbus software (version 2.8.2). Nucleoli were detected by using the ''B'' method. To compare independent experiments, the intensity of EU signal was normalized in each individual experiment as indicated in the figure legends. Data were plotted by using GraphPad Prism 10 software.

RNA-seq and data analyses

RNA samples were depleted of ribosomal RNAs with Ribo-Zero rRNA Removal Kit (#20040529; Illumina) and libraries prepared with NEBNext Ultra Directional RNA Library Prep Kit for Illumina (#E7420S; NEB) following manufacturer's instructions. RNA sequencing was performed on Illumina HiSeq4000 platform (pair-end 2 × 150 bp) at Biodiversa (Rovereto, TN, Italy). RNA-seq reads were quality checked with FastQC and trimmed with Cutadapt[121] using TrimGalore wrapper tool (Version 0.6.5). Libraries were then aligned to human genome (hg38 version) with HISAT2 aligner,[122] and read abundance over transcripts was computed with StringTie v2.0[123] tool using GENCODE (v36) gene reference. [124] StringTie v2.0 transcript estimations were imported in R v4.0.0 and converted to read count using Bioconductor tximport v1.16.1 package.[125] Read counts were batch corrected using the R package limma v3.44.3 library.[126] Differential expression and PCA analyses were performed using Bioconductor DESeq2 v1.28.1 package[127] with default settings. Differentially expressed (DE) genes were selected by adjusted p-value <0.00001 and fold change threshold of 1.5. Gene set over-representation analysis (GSOA) was performed using Bioconductor clusterProfiler v4.2.0 package[128] and MSigDB gene set database (version 7.2)[129] with default settings. Reactome and Gene Ontology terms from MSigDB were used in the analysis. GSOA used as input common up-regulated and downregulated genes in both SCAN1 clones vs. WT contrasts. Data plotting was performed using the Bioconductor tidyverse v1.3.0, enrichplot v1.8.1 packages and EnhancedVolcano v1.10.0 packages.

RNA/DNA hybrid slot blot

Slot blot experiments were performed as previously described.[31] Genomic nucleic acid isolation and RNase H (#M0297; NEB) treatment were carried out with the same procedure used for DRIP. Genomic nucleic acids were spotted into a Hybond-N^+ membrane and UV-crosslinked. The membrane was saturated and probed with S9.6 antibody (#MABE1095; Merck-Millipore) to detect RNA/DNA hybrids and an anti-dsDNA antibody (#ab27156; Abcam) to detect dsDNA, used as a loading control. Serial dilutions of genomic nucleic acids from U2OS WT cells were used to control that slot blot quantifications matched nucleic acid content. Images were acquired with a ChemiDoc MP Imaging System (Bio-Rad) and signals quantified using ImageLab software (version 6.0.1).

RNA/DNA hybrid quantification by immunofluorescence microscopy

Cells were seeded in 24 × 24 mm coverslips in a 35 mm dish at 2 x 10^5 cells per well. RNA/DNA hybrid staining was performed as described previously.[44,50] Briefly, 24 h after seeding, cells were fixed with ice-cold methanol for 10 min at RT and then acetone was added for 1 min on ice. Cells were washed three times with cold PBS and incubated for 30 min at RT in Block Buffer (4X Saline Sodium Citrate (SSC), 0.1% Tween 20, 3% BSA) under gentle rocking. Coverslips were then incubated with S9.6 antibody to stain for RNA/DNA hybrids (5 μg per coverslip), and anti-nucleolin antibody (#ab22758; Abcam) at 1/1,000 dilution for 2 h at RT. Glass slides were washed three times with 4X SSC and then incubated with secondary antibody Alexa Fluor 488 (Goat anti-Mouse IgG Secondary Antibody: #A-11001; ThermoFisher Scientific) and Alexa Fluor 594 (Goat anti-Rabbit IgG Secondary Antibody: #A-11037; ThermoFisher Scientific) for 1 h at RT. Coverslips were then washed three times with 4X SSC, incubated with DAPI (3.3 μg/mL in water) for 30 min and then mounted on microscope slides with Mowiol 4–88 (Merck-Millipore). Slides were imaged with a Nikon Eclipse 90i Microscope. Fluorescence quantification analysis was performed using ImageJ software (version1.53o). S9.6 intensity in the nucleoplasmic compartment was calculated by subtracting the nucleolar S9.6 signal from the total nuclear S9.6 signal.

DNA/RNA immunoprecipitation (DRIP)

DNA/RNA immunoprecipitation was carried out as described previously.[31,87,130] Briefly, non-crosslinked nuclei were isolated by lysing cells (85 mM KCl, 5 mM Pipes pH 8.0, 0.5% NP-40) and then, subjected to nuclear lysis (50 mM Tris-HCl pH 8.0, 5 mM EDTA, 1% SDS). Lysates were digested with proteinase K (#3115828001; Sigma-Aldrich) at 55°C for 3 h and genomic nucleic acids were precipitated with isopropanol followed by a wash in 75% ethanol. Where relevant, samples were treated with 1.7 U of RNase H (#M0297; NEB) per μg of genomic DNA for 5 h at 37°C. For spike-in controls in DRIP-qPCR, 6 μg of *Drosophila* S2 genomic nucleic acids were added to 20 μg of U2OS genomic nucleic acids prior to RNase H digestion. Next, genomic nucleic acids were sonicated with Bioruptor (Diagenode) in IP dilution buffer (16.7 mM Tris-HCl pH 8.0, 1.2 mM EDTA, 167 mM NaCl, 0.01% SDS, 1.1% Triton X-100) to obtain DNA fragments of about 500 bp. Samples were then precleared in presence of protease inhibitors (1X Complete mini EDTA-free protease; #11836170001; Sigma-Aldrich) with BSA-blocked protein A dynabeads (#10002D; Invitrogen). IP was performed with 2.5 μg of S9.6 antibody (#MABE1095; Merck-Millipore) or no antibody using 12.5 μg of precleared samples (13 μg for mixed U2OS and *Drosophila* S2 genomic nucleic acids) overnight at 4°C. Immunocomplexes were retrieved by incubation with BSA-blocked protein A dynabeads. Beads were then washed once with buffer A (20 mM Tris-HCl pH 8.0, 2 mM EDTA, 0.1% SDS, 1% Triton X-100, 0.15 M NaCl), once with buffer B (20 mM Tris-HCl pH 8.0, 2 mM EDTA, 0.1% SDS, 1% Triton X-100, 0.5 M NaCl), once with buffer C (10 mM Tris-HCl pH 8.0, 1 mM EDTA, 1% NP-40, 1% sodium deoxycholate, 0.25 M LiCl) and then twice with buffer D (10 mM Tris-HCl pH 8.0, 1 mM EDTA). Beads were then eluted in 1% SDS and 0.1 M NaHCO3 and eluates digested by proteinase K (#3115828001; Sigma-Aldrich) at 45°C for 2 h. DNA was purified with QIAquick PCR purification kit (#28104; QIAGEN) and analyzed by qPCR with IQ SYBR green Supermix (#1708880; Bio-Rad) in a CFX96 real-time system device (Bio-Rad). Bio-Rad CFX Manager 3.1 software was used for qPCR analysis. At a certain gene region, the amount of immunoprecipitated material was calculated as the percentage of input after subtracting the background signal (no antibody control). For DRIP-seq analysis, multiple S9.6 IPs with 3 μg of S9.6 antibody (#MABE1095; Merck-Millipore, lot#3695302, #3774162 and #3910138) were pooled and DNA was purified with MinElute PCR purification Kit (#28004; QIAGEN).

Library preparation and sequencing were performed by the Helixio company (Biopôle Clermont-Limagne, Saint-Beauzire, France) by using AVITI (Element Biosciences) with 150 bp paired-end reads. The primers used in this study are listed in Table S2.

DRIP-seq data processing

Raw data quality was checked with FastQC (v0.11.5) and then aligned to the human hg38 reference genome with BWA-MEM (v0.7.17).[131] Supplementary alignments (flag 2048), reads with mapping quality lower than 25 and PCR duplicates were removed using the samtools suite (v1.9)[132] and also for sorting and indexing BAMs. BamCoverage from Deeptools (v3.5.1)[133] was used to generate BigWig files with CPM normalization using the options: exactScaling, normalizeUsing CPM, binSize 1. First, we assessed the quality of the DRIP-seq datasets by meta-analysis of the *Z* score distribution over R-loop-forming sequences (RLFS) for IP samples (positive R-loop mapping) and Input samples (negative control), as described in Miller et al.[134] BigWig were first converted into bedGraph using bigWigToBedGraph tool and then peak calling was done using MACS3 bdgpeakcall (v3.0.0a6)[135] with parameters -g 1000 -c 5. RLSeq (v1.6.0) was used to generate metaplots of the *Z* score distribution around RLFS. All IP samples showed a *Z* score above 2 at 0 bp in the distribution, which was greater than both *Z* score at -5kb and +5kb, and had a permutation testing *p-value* below 0.04. All Input samples did not meet these criteria with a *Z* score around 0 at 0 bp in the distribution, and a permutation testing *p-value* above 0.38. The following *p-value*s were obtained: Rep1: $p < 0.0198$ for WT S9.6 IP, $p < 0.0198$ for SCAN1$^{\#1}$ S9.6 IP, $p < 0.42574$ for WT Input, $p < 0.39604$ for SCAN1$^{\#1}$ Input; Rep2: $p < 0.0396$ for WT S9.6 IP, $p < 0.0099$ for SCAN1$^{\#1}$ S9.6 IP, $p < 0.0099$ for SCAN1$^{\#2}$ S9.6 IP, $p < 0.44554$ for WT Input, $p < 0.47525$ for SCAN1$^{\#1}$ Input, $p < 0.38614$ for SCAN1$^{\#2}$ Input.

MACS3 callpeak (v3.0.0a6) with parameters -q 0.01 -f BAMPE were used on DRIP-seq BAM files and their inputs. Peaks were annotated on RefSeq genes using plyranges library in R (v4.2.1).[136] The following numbers of peaks were found: Rep1: 82,545 for WT S9.6 IP, 63,456 for SCAN1$^{\#1}$ S9.6 IP; Rep2: 89,445 for WT S9.6 IP, 110,745 for SCAN1$^{\#1}$ S9.6 IP, 89,932 for SCAN1$^{\#2}$ S9.6 IP. The following numbers of peaks overlapping annotated genes were: Rep1: 51,844 for WT S9.6 IP, 42,283 for SCAN1$^{\#1}$ S9.6 IP; Rep2: 51,645 for WT S9.6 IP, 64,908 for SCAN1$^{\#1}$ S9.6 IP, 51,932 for SCAN1$^{\#2}$ S9.6 IP.

DRIP-seq profiles show the number of aligned reads per base normalized by the total number of aligned reads (CPM) (Figures 2I, S3B–S3D and S3F). Read coverage is shown at different RefSeq gene loci, with only the first transcript variant per gene annotated.

For metagene profiles and boxplot analysis, the BED file used was downloaded using the AnnotationHub library and the id "AH100419" (hg38 NCBI RefSeq containing 26,089 genes, excluding chr. Y genes) and processed using the plyranges library in R. As the DRIP-seq experiments were not strand-specific, genes overlapping within a window of -1kb from their start to +1kb from their end were filtered out. The 11,048 remaining RefSeq genes were assigned to a corresponding ENSEMBL gene ID and a median FPKM for each condition (WT, SCAN1$^{\#1}$ and SCAN1$^{\#2}$), which was calculated from the 3 replicates of RNA-seq for each condition. org.Hs.e.g.db 3.17.0 was used to retrieve ENSEMBL ID from RefSeq, through AnnotationHub[137] and AnnotationDbi.[138] RefSeq genes were filtered out if no ENSEMBL ID could be assigned or if several ENSEMBL IDs correspond to one single RefSeq ID and conversely, giving 10,014 RefSeq genes left. Then, we filtered out genes with a median FPKM equal to 0 in all conditions (7,755 genes left). The differential expression analysis in SCAN1$^{\#1}$ and SCAN1$^{\#2}$ vs. WT cells was assigned for each RefSeq gene: Up-regulated (UP, 243) or Down-regulated (DOWN, 190) genes in both SCAN1 clones, and Non-regulated genes (Non-REG, 6,891) that were not differentially expressed in one and/or the other SCAN1 clones.

For Figures 2H and S3A, RefSeq genes with a length >100 nt (7,708 genes, including 243 UP, 190 DOWN and 6,844 Non-REG) were kept. ComputeMatrix scale-regions from Deeptools was used with parameters: binSize 100, regionBodyLength 10,000, afterRegionStartLength 2,000, beforeRegionStartLength 2,000. These parameters led to 20 bins between TSS-2kb to TSS, 100 bins on gene body and 20 bins on TES to TES+2kb regions. For each bin, the mean number of normalized aligned reads per base was computed. 7,703 RefSeq genes, including 243 UP, 190 DOWN and 6,839 Non-REG, showed a mean DRIP-seq coverage of all bins over the TSS to TES region >0 in at least one replicate for both WT IP and SCAN1$^{\#1}$ IP samples and were further used. Outliers (10 genes) showing a DRIP-seq mean coverage over the gene > to the 0.999% quantile in each IP sample were excluded. The final 7,693 analyzed genes included 243 UP, 190 DOWN and 6,830 Non-REG. Their mean DRIP-seq coverage of all bins over the TSS to TES region was used for Figures 2H and S3A.

For Figures S3H–S3J, RefSeq genes with a length >3 kb (7,115 genes, including 235 UP, 179 DOWN and 6,289 Non-REG) were kept. ComputeMatrix scale-regions from Deeptools was used with parameters: binSize 100, regionBodyLength 10,000, afterRegionStartLength 2,000, beforeRegionStartLength 4,000. These parameters led to 40 bins between TSS-2kb to TSS+2kb, 100 bins on gene body and 20 bins on TES to TES+2kb regions. For each bin, the mean number of normalized aligned reads per base was computed. 7,113 RefSeq genes, including 235 UP, 179 DOWN and 6,288 Non-REG, showed a mean DRIP-seq coverage of all bins over the TSS to TES region >0 in at least one replicate for both WT IP and SCAN1$^{\#1}$ IP samples and were then used. Outliers showing a DRIP-seq mean coverage over the gene > to the 0.999% quantile in each IP sample were excluded and corresponded to 15 genes. The final 7,098 analyzed genes included 233 UP, 179 DOWN and 6,276 Non-REG. In Figure S3J, the metagene profiles for the 233 UP genes were generated by plotting the mean DRIP-seq coverage within the gene population for each bin. For boxplot analyses in Figures S3H and S3I, the mean DRIP-seq coverage of all bins over the described regions (TSS to TSS+2kb and TSS+2kb to TES) was calculated for each gene.

For graphical representation of DRIP-seq signal changes (Log2(SCAN1/WT)) in Figures 2H, S3A, S3H and S3I, we used box-and-whisker plots with GraphPad Prism 10 software with the following settings: boxes: 25–75 percentile range; whiskers: 5–95 percentile range; horizontal bars: median.

Immunofluorescence microscopy of γH2AX, p53BP1 and micronuclei

For DSB immunostaining, cells were seeded in poly-L-lysine (#P4832; Sigma-Aldrich)-coated 96-well plates (CellCarrier Ultra, #6005550 or Phenoplate, #6055300; PerkinElmer). To label newly synthesized DNA in replicating cells, cells were incubated with 10 μM EdU for 30 min. When treated with CPT, cells were first incubated with 10 μM EdU for 30 min or co-incubated with 10 μM EdU with either 50 μM DRB or 10 μM MG132 for 1 h, then CPT (0.1, 5, 10 or 25 μM) was added for an additional hour while maintaining EdU, EdU/DRB, or EdU/MG132 in the media. For the CPT release experiments, after 1 h CPT treatment, cells were washed four times and incubated in medium with 10 μM EdU for the indicated times. Cells were washed twice with PBS and fixed with 3.7% formaldehyde for 15 min. After two washes with PBS, cells were permeabilized with 0.5% Triton X-100 for 20 min and washed twice with PBS. The incorporated EdU into DNA was detected using the Click-iT reaction from the Click-iT EdU Alexa Fluor 647 Imaging Kit (#C10340; ThermoFisher Scientific) according to the manufacturer's protocol. After a wash with 3% BSA in PBS, cells were incubated with 8% BSA in PBS for 1 h. For γH2AX and/or p53BP1 staining, cells were incubated with a mouse anti-γH2AX antibody (#05–636; Merck-Millipore) and/or a rabbit anti-p53BP1 antibody (#2675; Cell Signaling Technology) diluted at 1/500 in 1% BSA in PBS for 2 h. For γH2AX and CENPF co-staining, cells were incubated with a rabbit anti-γH2AX antibody (#9718S; Cell Signaling Technology) and a mouse anti-CENPF antibody (#135865; Santa Cruz Biotechnology) diluted at 1/500 and 1/100, respectively, in 1% BSA in PBS for 2 h. After three washes with PBS, cells were incubated with the appropriate secondary antibody coupled to Alexa Fluor 488 or 594 (ThermoFisher Scientific) diluted at 1/500 in 1% BSA in PBS for 1 h. Cells were washed three times with PBS and nuclei were stained with 1 μg/mL Hoechst 33342 (ThermoFisher Scientific) for 15 min, washed twice with PBS and stored at 4°C until imaging.

96-well plates were scanned with a 20× objective using an Operetta CLS High-Content Imaging System (PerkinElmer) with Harmony software (version 4.9). Analyses of γH2AX, p53BP1, CENPF and micronuclei were performed with Columbus software (version 2.8.2). γH2AX and p53BP1 foci were detected with the function ''Find spots'' and the ''C'' method. Variations of the number of foci between independent experiments can be related to experimental variabilities, which include the automatic counting of foci with

Columbus software that depends on the ratio between the signal intensity of foci and background noise. To compare independent experiments, the number of γH2AX or p53BP1 foci were normalized in each individual experiment as indicated in the figure legends. Micronuclei were detected using the Hoechst 33342 staining with the function ''Find Micronuclei'' and the ''B'' method. Throughout the manuscript, G1 cells were identified as EdU-negative and low Hoechst 33342, S cells as EdU-positive, and G2 cells as EdU-negative and high Hoechst 33342. When indicated, G1 cells were identified as EdU-negative and CENPF-negative, S cells as EdU-positive, and G2 cells as EdU-negative and CENPF positive. For the CPT release experiments to analyze DSB repair, the percentages of γH2AX/p53BP1 foci or γH2AX intensity remaining following CPT removal were calculated by subtracting the number of foci or intensity of untreated cells from that of treated cells and normalized to cells treated with CPT.

For graphical representation of foci or intensity distribution, we used box-and-whisker plots with GraphPad Prism 10 software with the following settings: boxes: 25–75 percentile range; whiskers: 10–90 percentile range; horizontal bars: median number of foci; ''+'': mean number of foci.

Proximity ligation assay (PLA)

Cells were seeded on 14 mm diameter coverslips. To label newly synthesized DNA, cells were incubated with 10 μM EdU for 30 min. After two washes with PBS, cells were pre-extracted with cold 0.5% NP-40 for 3 min on ice to remove nucleosoluble proteins as reported.[139] After one wash in PBS, cells were fixed with 3.7% formaldehyde in PBS for 15 min, washed twice with PBS and permeabilized with 0.2% Triton X-100 in PBS for 20 min. Cells were washed twice in PBS, then the incorporated EdU into DNA was detected using the Click-iT reaction from the Click-iT EdU Alexa Fluor 647 Imaging Kit (#C10340, ThermoFisher Scientific) according to the manufacturer's protocol. Following two washes in PBS, cells were blocked with 8% BSA in PBS for 1 h. The following steps were performed according to the Duolink (Sigma-Aldrich) manufacturer's instructions. Cells were incubated with a rabbit anti-TOP1 antibody (#ab10937; Abcam) diluted at 1/250 in Duolink antibody dilution buffer and/or a mouse S9.6 antibody (#MABE1095; Merk-Millipore) diluted at 1/200 in Duolink antibody dilution buffer overnight at 4°C. Then, cells were incubated in a solution containing PLA probe anti-mouse minus (#DUO92004; Sigma-Aldrich) and PLA probe anti-rabbit plus (#DUO92002; Sigma-Aldrich) for 1 h at 37°C. The Duolink *In Situ* Detection Reagents Green (#DUO92014; Sigma-Aldrich) were then used to perform the PLA reaction. Slides were mounted in Duolink *In Situ* Mounting Medium with DAPI (#DUO82040; Sigma-Aldrich) and images were acquired with an inverted microscope (AxioObserver Z1 fluorescence microscope; ZEISS) using a 40× oil immersion objective. The number of PLA foci was quantified using ImageJ software (version 1.53o) in G1 cells identified as EdU-negative and low Hoechst 33342, and S cells identified as EdU-positive.

Box-and-whisker plots with GraphPad Prism 10 software were used for graphical representation, with the following settings: boxes: 25–75 percentile range; whiskers: 10–90 percentile range; horizontal bars: median number of foci; ''+'': mean number of foci.

siRNA transfections

WI38-hTERT cells were transfected with siRNA duplexes using Dharmafect 4 transfection reagent (#T-2004; Dharmacon/Horizon Discovery) for 24 h before inducing quiescence for 72 h, as described previously.[31] U2OS cells were transfected with siRNA duplexes using Lipofectamine RNAiMAX transfection reagent (#13778075; ThermoFisher Scientific) for 72 h according to the manufacturer's instructions. siRNAs used are from Dharmacon/Horizon Discovery and are pools of 4 siRNAs per gene (DNA ligase 3: M-009227-02; DNA ligase 4: M-004254-00; PARP1: M-006656-01; PNKP: M-006783-02; TDP1: M-016112-01; TDP2: M-017578-00; XPF: M-019946-00; XRCC1: M-009394-01; XRCC4: M-004494-02), or are individual siRNAs (firefly luciferase control sequence: D-001400-01).

Co-immunoprecipitation experiments

Co-immunoprecipitation (coIP) was performed as described previously.[87] HEK293T cells were transfected in 6-well plates 24 h after seeding with 2 μg of DNA plasmid mix containing 0.2 μg of each plasmid (as indicated in Figure 6H) and empty vector pEF-myc-cyto (up to 2 μg) using JetPRIME (#101000046; Polyplus Transfection) manufacturer's instruction. Cells were pelleted 24 h after transfection and incubated with lysis buffer (50 mM Tris-HCl pH 8.0, 150 mM NaCl, 1% NP-40, 10% glycerol, 2.5 mM MgCl2) supplemented with 1X Complete mini EDTA-free protease (#11836170001; Sigma-Aldrich) and 1X phosphatase (PhosSTOP: #04906845001; Roche) inhibitors and 40 U benzonase (#E1014; Sigma-Aldrich) at 4°C for 30 min. Samples were diluted 1:2 in dilution buffer (150 mM NaCl, 10% glycerol, 2.5 mM MgCl2) supplemented with 1X Complete mini EDTA-free protease (#11836170001; Sigma-Aldrich) and 1X phosphatase (PhosSTOP: #04906845001; Roche) inhibitors after centrifugation to remove insoluble material. IP was carried out from 500 μg of proteins with Nanobody ALFA-coupled agarose beads (ALFA Selector ST: #N1511; NanoTag Biotechnologies) or agarose beads without antibody (Selector Control: #N0010; NanoTag Biotechnologies) at 4°C on rotating wheel for 2 h. Immuno-complexes were washed three times with IP buffer (1:1 lysis and dilution buffers) and three times with IP buffer without NP-40, in presence of 1X Complete mini EDTA-free protease inhibitors (#11836170001; Sigma-Aldrich) and eluted in 1X LDS (Invitrogen) with 100 mM DTT for 10 min at 70°C. Proteins were separated by SDS-PAGE and immunoblotted with the following antibodies at dilutions recommended by the manufacturer: anti-ALFA (#N1501-HRP; NanoTag Biotechnologies), anti-FLAG (#MA1-91878; Invitrogen), anti-GFP (#ab290; Abcam), anti-HA (#2999; Cell Signaling) and anti-Myc (#13–2500; Invitrogen). Immunoblotting was revealed by chemiluminescence using a ChemiDoc MP Imaging System (Bio-Rad).

BRET2 titration curves and competition assays

For all BRET experiments (titration curves and competition assays), 650,000 HEK293T cells were seeded in each well of 6-well plates. After 24 h at 37°C, cells were transfected with a total of 1.6 μg of DNA mix, containing the donor + acceptor ± competitor plasmids, using JetPRIME transfection reagent (# 101000046; Polyplus Transfection). For the BRET donor saturation assays, cells were transfected with 0.025 μg of donor (LIG3α) and with an increased amount of acceptor plasmid (0.025, 0.05, 0.1, 0.25, 0.375, 0.5 and 0.75 μg of DNA) equalized to a total amount of 1.6 μg of DNA with an empty vector pEF-myc-cyto. In dose-response competition experiments, competitors were transfected with the following amount of DNA: 0.125, 0.5, and 1.25 μg with a 1:10 donor:acceptor DNA plasmid ratio (i.e., 0.025 μg:0.25 μg of DNA plasmid). Cells were detached 24 h later, washed with PBS, and seeded in a white 96-well plate (clear bottom, #6005181; PerkinElmer) in Opti-MEM without phenol red medium complemented with 4% FBS, and cells were incubated for an additional 20 to 24 h at 37°C before the BRET assay reading. A step-by-step BRET protocol is provided elsewhere.[140]

BRET2 measurements

BRET2 signal was determined immediately after injection of coelenterazine 400a substrate (10 μM final concentration) to cells (#16157; Cayman Chemicals) using a CLARIOstar instrument (BMG Labtech) with a luminescence module. Total GFP2 fluorescence was detected with excitation and emission peaks set at 400 ± 15 and 510 nm ± 20, respectively. Total RLuc8 luminescence was measured with an emission peak set at 480 nm ± 80.

The BRET signal or BRET ratio corresponds to the light emitted by the GFP2 acceptor constructs (515 nm ± 30) upon addition of coelenterazine 400a divided by the light emitted by the RLuc8-LIG3α donor construct (410 nm ± 80). The background signal is subtracted from that BRET ratio using the donor-only negative control where only the RLuc8-LIG3α fusion plasmid is transfected into the cells. The normalized BRET ratio is the BRET ratio normalized to the no competitor control during a competition assay.

QUANTIFICATION AND STATISTICAL ANALYSIS

Information on independent biological replicates (*n*), statistical tests, definition of center (mean, median) and dispersion (SD, SEM), are indicated in the figure legends. For immunofluorescence microscopy experiments, an average of ≥1,000 nuclei per experiment and per condition were analyzed when using the Operetta/Columbus system and between 30 and 40 (Figures 3G and S4J), 45 (Figures 1F and S6B) and 100 nuclei (Figure 2G) when using ImageJ. Experimental differences were tested for significance by using GraphPad Prism 10 software. Ns indicates not significant differences. $p < 0.05$ is considered significant. $^{*}p < 0.05$, $^{**}p < 0.01$, $^{***}p < 0.001$, $^{****}p < 0.0001$.